TANNEHILL AND HOLST
FEBRUARY 1974

Final Report — Part II
ISU — ERI — AMES — 74057

NUMERICAL COMPUTATION OF TWO-DIMENSIONAL VISCOUS BLUNT BODY FLOWS WITH AN IMPINGING SHOCK

Project 930-S

ENGINEERING
RESEARCH
ENGINEERING
RESEARCH
ENGINEERING
RESEARCH
ENGINEERING
RESEARCH
ENGINEERING
RESEARCH

FINAL REPORT - PART II

NUMERICAL COMPUTATION OF TWO-DIMENSIONAL VISCOUS BLUNT BODY FLOWS WITH AN IMPINGING SHOCK

T. L. HOLST

J. C. TANNEHILL

FEBRUARY 1974

ISU — ERI — AMES — 74057
Project 930-S

ENGINEERING   RESEARCH   INSTITUTE

IOWA STATE UNIVERSITY   AMES

TABLE OF CONTENTS

Page Intentionally Left Blank

NUMERICAL COMPUTATION OF TWO-DIMENSIONAL VISCOUS

BLUNT BODY FLOWS WITH AN IMPINGING SHOCK

John C. Tannehill and Terry L. Holst
Iowa State University

SUMMARY

Two-dimensional viscous blunt body flows with an impinging shock
have been computed using a "time-dependent" finite-difference method which
solves the complete set of Navier-Stokes equations for a compressible
flow. For low Reynolds number flows, the entire flow field, including
the bow shock and impinging shock, has been "captured" in the computa-
tion. For higher Reynolds number flows, the bow shock is treated as a
discontinuity across which the Rankine-Hugoniot equations are applied,
while the boundary layer and interaction regions are "captured" as
before. Using this latter "shock-fitting" approach, a Type III shock
interaction flow field has been computed with flow conditions
corresponding to the Space Shuttle Orbiter freestream conditions at
61 km (200,000 ft).

NOTATION

c_p = specific heat at constant pressure

C = constant in Sutherland's equation

D = diameter of cylinder

e = specific internal energy

E = total energy

$\bar{i}_r$ = unit vector in radial direction

$\bar{i}_\theta$ = unit vector in transverse direction

k = coefficient of thermal conductivity

K = local radius of curvature

Kn = Knudsen number

M = Mach number

$\bar{n}_s$ = outward unit normal to bow shock

p = pressure

Pr = Prandtl number, $c_p \mu/k$

q_j = heat flux vector

r_s = local radius of bow shock

r_{s_t} = local radial shock velocity

r_{s_θ} = $\partial r_s/\partial \theta$

R = gas constant

Re_D = Reynolds number based on diameter

t = time

$\bar{t}$ = transformed time

u = tangential velocity component

Page Intentionally Left Blank

U_s = local shock velocity

v = normal velocity component

V_1 = fluid velocity normal to shock

y = transformed coordinate given by Eq. (16)

$\bar{y}$ = transformed coordinate given by Eq. (14)

z = transformed coordinate given by Eq. (16)

$\bar{z}$ = transformed coordinate given by Eq. (14)

α = transformation parameter in Eq. (A1)

β = stretching factor in Eq. (16)

β' = stretching factor in Eq. (A1)

γ = specific heat ratio

δ = local distance between body and outer boundary

η = coordinate measured normal to body

θ = angle measured from stagnation streamline

μ = viscosity coefficient

ζ = coordinate measured along body

ρ = density

τ_{ij} = shear stress tensor

Subscripts

1 = undisturbed conditions ahead of impinging shock

2 = conditions behind impinging shock

j = mesh point location in z direction

k = mesh point location in y direction

stag = stagnation point value without impingement

t = total condition

w = wall value

∞ = freestream value

Superscript

n = time step location

INTRODUCTION

An extraneous shock impinging on a blunt body in a hypersonic flow
has been observed to greatly increase both the heat transfer rate and
pressure near the impingement point. In fact, Hains and Keyes[1] have
measured peak heating rates up to 17 times the ordinary stagnation
point rate and pressure peaks up to 8 times the freestream pitot pressure
as a result of shock impingement. Flow fields of this type will occur
on the Space Shuttle and other maneuverable re-entry vehicles. For
example, high heating rates and pressures can be expected on the Space
Shuttle Orbiter at the point where the bow shock from the nose intersects
the blunt leading edge of the wing if the sweep angle is not large
enough.

The intense heating and high pressures described above occur over
a small region where a disturbance, originating at the intersection of
the impinging shock and bow shock, strikes the body. The disturbance
may be a free shear layer, a supersonic jet, or a shock depending on the
location of the impinging shock and the shape of the body. Edney[2] has
described six different types of shock interference patterns, which
include the various kinds of disturbances. The shock interference
pattern which produces the maximum heating rates and pressures is Type IV,
which is shown in Fig. 1. In this type of interference pattern, the
disturbance is a supersonic jet which is embedded in the subsonic
portion of the flow field.

During the present study, two-dimensional shock impingement flow

fields have been computed using a "time-dependent," finite-difference

method which solves the complete set of Navier-Stokes equations for a

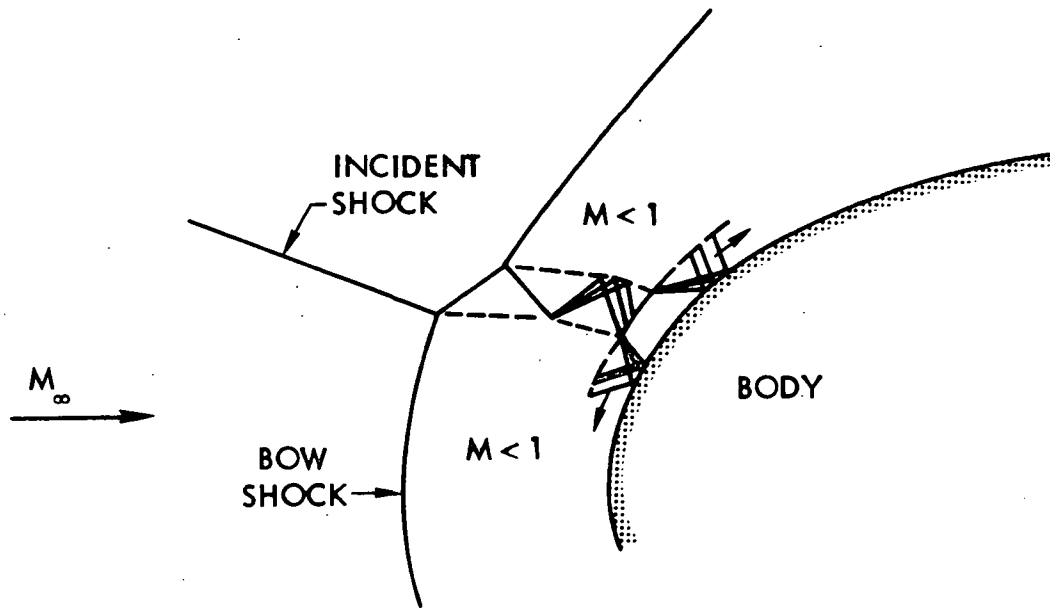compressible flow. The major advantage of the "time-dependent" method is

Fig. 1. Type IV shock interference pattern.

that the resulting unsteady Navier-Stokes equations are a mixed set of

hyperbolic-parabolic equations for both subsonic and supersonic flows.

As a result, a very complicated flow field, such as the one shown in

Fig. 1 where both subsonic and supersonic regions are present, can be

calculated as an initial-value problem. An additional advantage is that

since the Navier-Stokes equations are solved in a conservative manner,

shocks are automatically allowed to form without previous knowledge of

their location or even existence.

For low Reynolds number flows, the entire flow field, including the bow shock, can be "captured" using the so-called "shock-capturing" approach. The computational domain for this type of calculation is shown in Fig. 2. For higher Reynolds number flows, it is not practical to
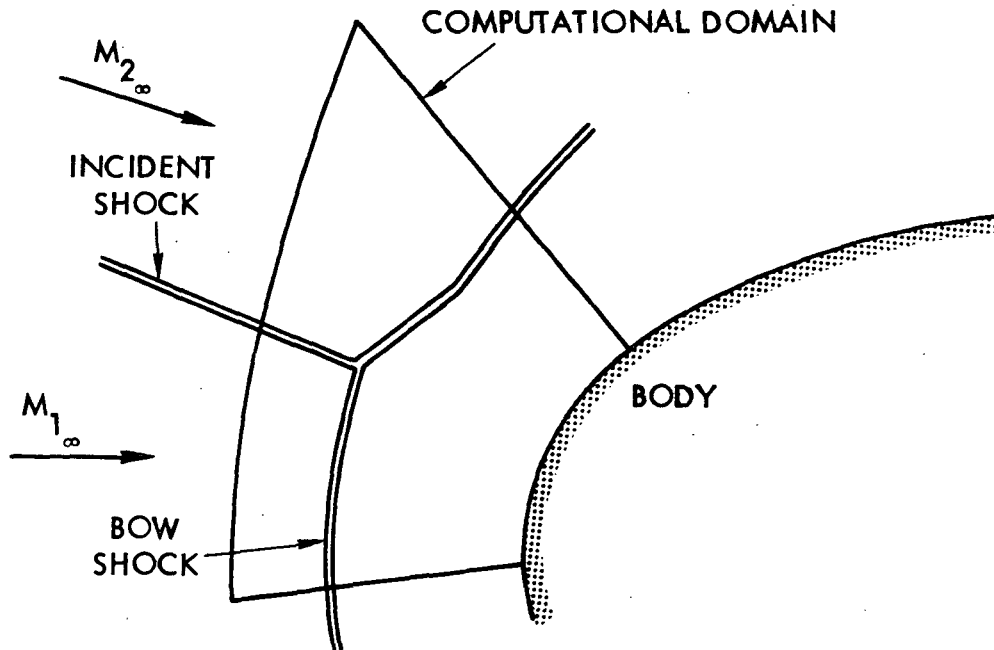

Fig. 2. Computational domain for "Shock-Capturing" method.

"capture" the bow shock because of the numerical difficulties associated with the large gradients at the bow shock. Instead, it is more convenient to treat the bow shock as a discontinuity, across which the Rankine-Hugoniot equations can be applied, while leaving the boundary layer and interaction regions to be captured as before. This latter approach is the so-called "shock-fitting" method. The computational domain for this method is shown in Fig. 3. In the present study, both the "shock-capturing" and "shock-fitting" methods have been used to
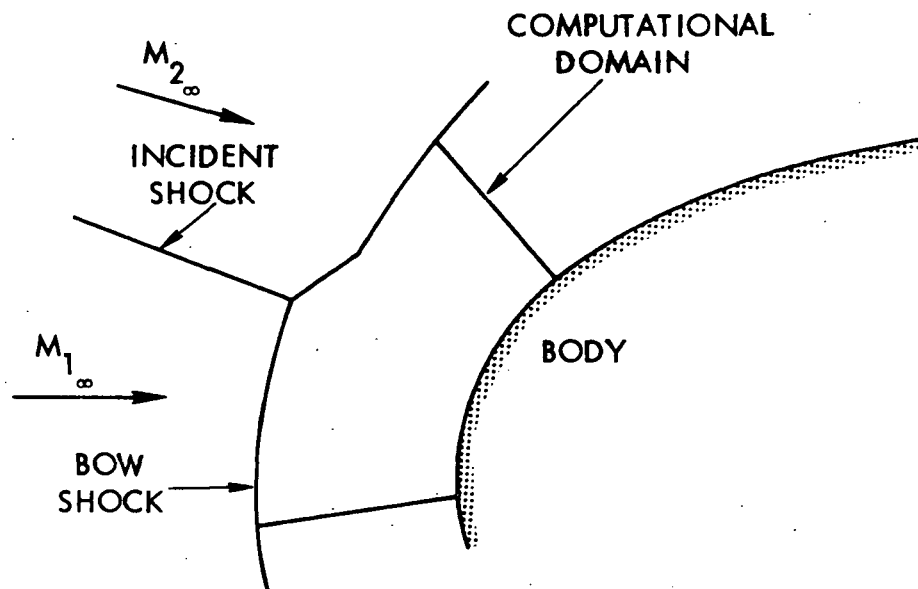
Fig. 3. Computational domain for "Shock-Fitting" method .

compute two-dimensional viscous blunt body flows with an impinging shock.
Thus far, numerical difficulties have prevented the computation of
Edney's Type IV shock interference patterns. However, Type III inter-
actions have been successfully computed in this study.

GOVERNING EQUATIONS

The fundamental governing equations for an unsteady flow without body forces or external heat additions can be written in conservation-law form for a two-dimensional body, intrinsic coordinate system (see Fig. 4) as[3]

$$\frac{\partial \bar{U}}{\partial t} + \frac{\partial \bar{F}}{\partial \xi} + \frac{\partial \bar{G}}{\partial \eta} + \bar{H} = 0 \tag{1}$$

where

$$\bar{U} = (1 + K\eta) \begin{bmatrix} \rho \\ \rho u \\ \rho v \\ E \end{bmatrix} \tag{2}$$

$$\bar{F} = \begin{bmatrix} \rho u \\ p + \rho u^2 - \tau_{\xi\xi} \\ \rho uv - \tau_{\xi\eta} \\ Eu + pu + q_\xi - u\tau_{\xi\xi} - v\tau_{\xi\eta} \end{bmatrix} \tag{3}$$

$$\bar{G} = (1 + K\eta) \begin{bmatrix} \rho v \\ \rho uv - \tau_{\eta\xi} \\ p + \rho v^2 - \tau_{\eta\eta} \\ Ev + pv + q_\eta - u\tau_{\eta\xi} - v\tau_{\eta\eta} \end{bmatrix} \tag{4}$$

$$\overline{H} = \begin{bmatrix} 0 \\ K(\rho u v - \tau_{\xi\eta}) \\ -K(p + \rho u^2 - \tau_{\xi\xi}) \\ 0 \end{bmatrix} \tag{5}$$

and E is the total energy given by

$$E = \rho\left(e + \frac{u^2 + v^2}{2}\right) \tag{6}$$

In addition to the above conservation equations, an equation of state in the form

$$p = p(e, \rho) \tag{7}$$

must be specified. For a perfect gas, this equation can be written as

$$p = (\gamma - 1)\rho e \tag{8}$$

For the case of air in chemical equilibrium, approximate curve fits are available for Eq. (7) in Refs. 4 and 5.
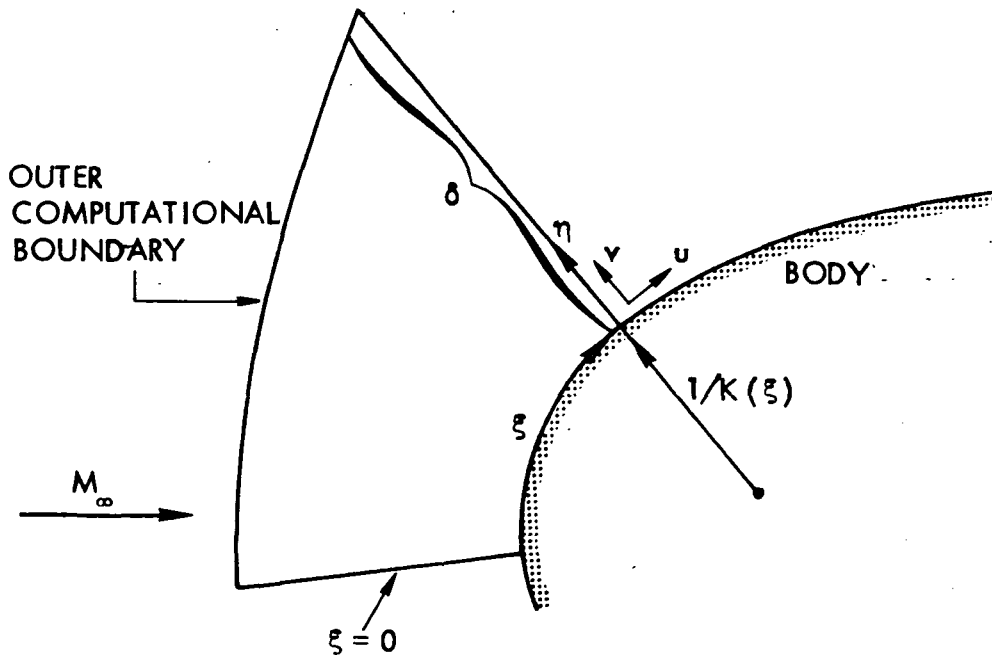

Fig. 4. Two-dimensional body intrinsic coordinate system.

In the present study, the Navier-Stokes expressions were used for the shearing stress tensor and heat flux vector; thus the components of the shearing stress tensor and heat flux vector are .

$$\tau_{\xi\xi} = \mu e_{\xi\xi} - \frac{1}{3}\mu(e_{\xi\xi} + e_{\eta\eta})$$

$$\tau_{\eta\eta} = \mu e_{\eta\eta} - \frac{1}{3}\mu(e_{\xi\xi} + e_{\eta\eta}) \tag{9}$$

$$\tau_{\xi\eta} = \mu e_{\xi\eta}$$

where

$$e_{\xi\xi} = \frac{2}{1 + K\eta}\left(\frac{\partial u}{\partial \xi} + Kv\right)$$

$$e_{\eta\eta} = 2\left(\frac{\partial v}{\partial \eta}\right) \tag{10}$$

$$e_{\xi\eta} = \left(\frac{1}{1 + K\eta}\right)\left(\frac{\partial v}{\partial \xi}\right) + \frac{\partial u}{\partial \eta} - \left(\frac{Ku}{1 + K\eta}\right)$$

and

$$q_\xi = \frac{-k}{1 + K\eta}\frac{\partial T}{\partial \xi}$$

$$\tag{11}$$

$$q_\eta = -k\frac{\partial T}{\partial \eta}$$

In order to complete the system of equations, it is necessary to specify expressions for the viscosity (μ) and the coefficient of thermal

conductivity (k). For all of the present computations, Sutherland's equation

$$\mu = \mu_\infty \left(\frac{T}{T_\infty} \right)^{\frac{1}{2}} \frac{1 + C/T_\infty}{1 + C/T} \tag{12}$$

was used to determine the viscosity, and the coefficient of thermal conductivity was computed by assuming a constant Prandtl number:

$$k = \frac{\gamma \, R \mu}{(\gamma - 1)Pr} \tag{13}$$

Approximate curve fits for μ and k suitable for "time-dependent" computations are presently being developed for the case of air in chemical equilibrium.

Two independent variable transformations are applied to the governing equations listed above. The first transformation maps the computational domain shown in Fig. 4 into a rectangular region in the transformed $(\bar{y}, \bar{z})$ plane. The outer computational boundary in Fig. 4 is either the bow shock (for a "shock-fitting" computation) or a freestream boundary (for a "shock-capturing" computation). The equations of the first independent variable transformation are:

$$\bar{y} = \xi$$

$$\bar{z} = 1 - \frac{\eta}{\delta} \tag{14}$$

$$\bar{t} = t$$

where $\delta = \delta(\xi, t)$ for a "shock-fitting" computation and $\delta = \delta(\xi)$ for a

"shock-capturing" computation. The relations between the partial derivatives are given by

$$\frac{\partial}{\partial \xi} = \frac{\partial}{\partial \bar{y}} + (1 - \bar{z}) \frac{\delta \bar{y}}{\delta} \frac{\partial}{\partial \bar{z}}$$

$$\frac{\partial}{\partial \eta} = -\frac{1}{\delta} \frac{\partial}{\partial \bar{z}} \qquad (15)$$

$$\frac{\partial}{\partial t} = \frac{\partial}{\partial \bar{t}} + (1 - \bar{z}) \frac{\delta \bar{t}}{\delta} \frac{\partial}{\partial \bar{z}}$$

The second independent variable transformation stretches the computational mesh in the direction normal to the body so that the mesh may be refined either near the body or near the outer computational boundary. By refining the mesh near the body, it is possible to describe the boundary layer more accurately. On the other hand, it may be desirable to refine the mesh near the outer boundary for shock impingement computations, although the results from initial computations tend to dispute this. The equations of this transformation, which were previously used by Li[6], are

$$y = \bar{y}$$

$$z = \frac{1 - e^{\beta \bar{z}}}{1 - e^{\beta}} \qquad (16)$$

$$t = \bar{t}$$

The amount and type of stretching is determined by the value of β. If β

equals zero there is no stretching. If β is greater than zero the mesh is refined near the body, and if β is less than zero the mesh is refined near the outer computational boundary.

The relations between the partial derivatives for this second transformation are given by

$$\frac{\partial}{\partial \bar{y}} = \frac{\partial}{\partial y}$$

$$\frac{\partial}{\partial \bar{z}} = \frac{-\beta e^{\beta \bar{z}}}{1 - e^{\beta}} \frac{\partial}{\partial z} \qquad (17)$$

$$\frac{\partial}{\partial \bar{t}} = \frac{\partial}{\partial t}$$

An alternative to the present transformation is given in Appendix A. This alternate transformation makes use of a logarithmic function which has been found to give better computational results when an impinging shock is present.

After employing the two transformations given by Eqs. (14) and (16), the final computational grid in the (y,z) plane is shown in Fig. 5 and the corresponding grid in the physical plane (ξ, η) is shown in Fig. 6 for β > 0. The final forms of the governing equations are

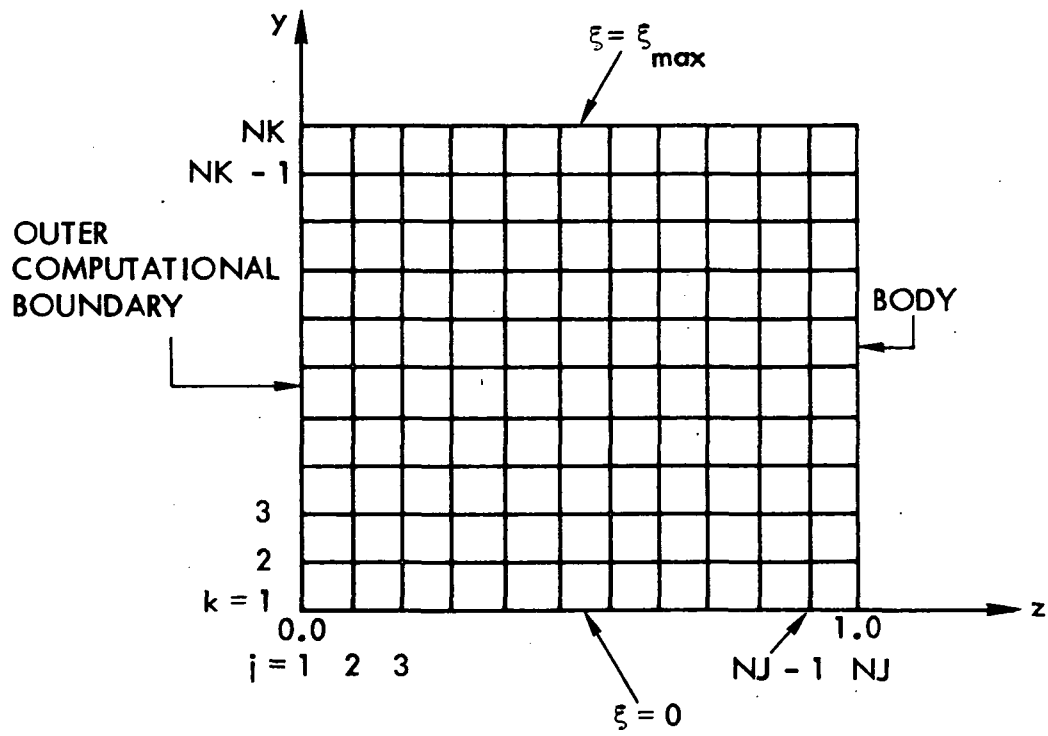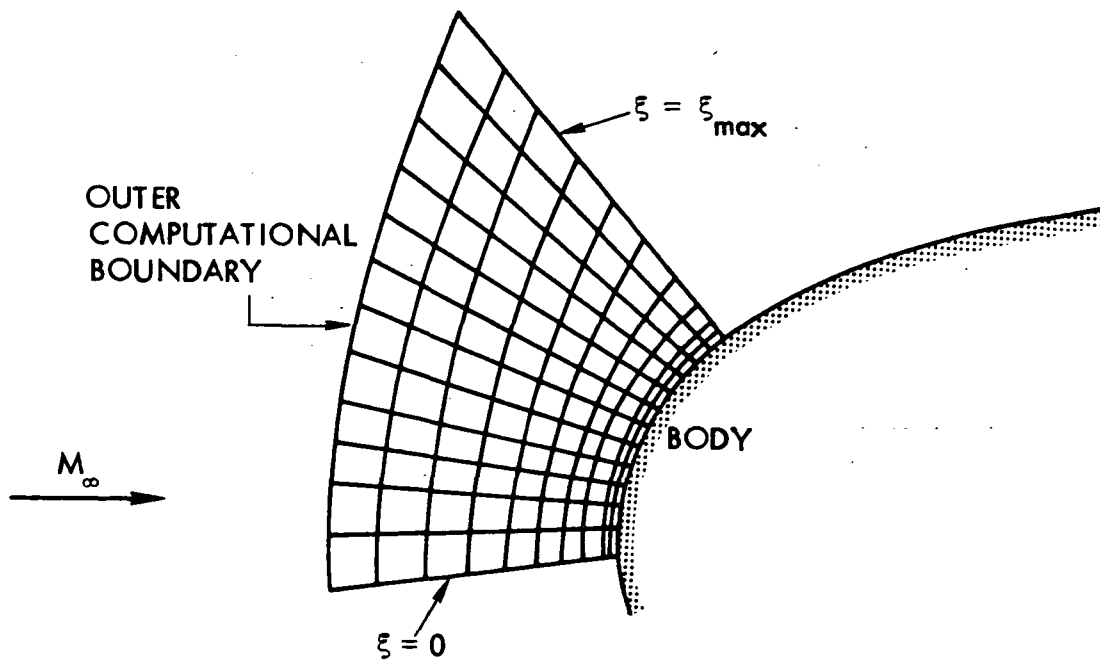$$\frac{\partial U}{\partial t} + \frac{\partial F}{\partial y} + \frac{\partial G}{\partial z} + H = 0 \qquad (18)$$

Fig. 5. Computational plane

Fig. 6. Physical plane ($\beta > 0$)

$$U = \left[\delta + \delta^2 K(1 - \bar{z})\right] \begin{bmatrix} \rho \\ \rho u \\ \rho v \\ E \end{bmatrix} \tag{19}$$

$$F = \delta \begin{bmatrix} \rho u \\ p + \rho u^2 - \tau_{yy} \\ \rho uv - \tau_{yz} \\ Eu + pu + q_y - u\tau_{yy} - v\tau_{yz} \end{bmatrix} \tag{20}$$

$$G = \frac{\beta e^{\beta \bar{z}}}{(1 - e^{\beta})} \left[1 + K\delta(1 - \bar{z})\right] \begin{bmatrix} \rho v \\ \rho uv - \tau_{yz} \\ p + \rho v^2 - \tau_{zz} \\ Ev + pv + q_z - u\tau_{yz} - v\tau_{zz} \end{bmatrix} - \frac{\beta e^{\beta \bar{z}}}{(1 - e^{\beta})} \frac{(1 - \bar{z})}{\delta} (\delta_y F + \delta_t U) \tag{21}$$

$$H = \delta \begin{bmatrix} 0 \\ K(\rho uv - \tau_{yz}) \\ -K(p + \rho u^2 - \tau_{yy}) \\ 0 \end{bmatrix} + \left(\frac{1 - e^{\beta}}{e^{\beta \bar{z}}}\right) G \tag{22}$$

$$\tau_{yy} = \frac{2}{3} \mu e_{yy} - \frac{1}{3} \mu e_{zz}$$

$$\tau_{zz} = \frac{2}{3} \mu e_{zz} - \frac{1}{3} \mu e_{yy} \tag{23}$$

$$\tau_{yz} = \mu e_{yz}$$

$$e_{yy} = \left(\frac{2}{1 + K\delta(1-\bar{z})} \right) \left[\frac{\partial u}{\partial y} - (1 - \bar{z}) \frac{\delta_y}{\delta} \frac{\beta e^{\beta \bar{z}}}{(1-e^{\beta})} \frac{\partial u}{\partial z} + Kv \right]$$

$$e_{zz} = \frac{2\beta e^{\beta \bar{z}}}{\delta(1-e^{\beta})} \frac{\partial v}{\partial z} \tag{24}$$

$$e_{yz} = \frac{1}{1+K(1-\bar{z})\delta} \left[\frac{\partial v}{\partial y} - \frac{(1-\bar{z})\delta_y \beta e^{\beta \bar{z}}}{(1-e^{\beta})\delta} \frac{\partial v}{\partial z} \right] + \frac{\beta e^{\beta \bar{z}}}{(1-e^{\beta})\delta} \frac{\partial u}{\partial z} - \frac{Ku}{1+K(1-\bar{z})\delta}$$

$$q_y = \left[\frac{-k}{1+K(1-\bar{z})\delta} \right] \left[\frac{\partial T}{\partial y} - \frac{(1-\bar{z})\delta_y \beta e^{\beta \bar{z}}}{(1-e^{\beta})\delta} \frac{\partial T}{\partial z} \right] \tag{25}$$

$$q_z = \frac{-k\beta e^{\beta \bar{z}}}{(1-e^{\beta})\delta} \frac{\partial T}{\partial z}$$

where

$$\bar{z} = \frac{1}{\beta} \ell n \left[1 - z(1-e^{\beta}) \right] \tag{26}$$

NUMERICAL SOLUTION OF EQUATIONS

Finite-Difference Scheme

MacCormack's finite-difference scheme[7,8] is used to solve the govern-
ing equations at each interior grid point. This explicit, two-step
scheme has second-order accuracy in both space and time. When
MacCormack's algorithm is applied to Eq. (18), the following predictor-
corrector equations result

$$\overline{U}_{j,k}^{n+1} = U_{j,k}^{n} - \frac{\Delta t}{\Delta y}(F_{j,k+1}^{n} - F_{j,k}^{n}) - \frac{\Delta t}{\Delta z}(G_{j+1,k}^{n} - G_{j,k}^{n}) - \Delta t\, H_{j,k}^{n} \tag{27}$$

and

$$U_{j,k}^{n+1} = \frac{1}{2}\left[U_{j,k}^{n} + \overline{U}_{j,k}^{n+1} - \frac{\Delta t}{\Delta y}\left(\overline{F}_{j,k}^{n+1} - \overline{F}_{j,k-1}^{n+1}\right) - \frac{\Delta t}{\Delta z}\left(\overline{G}_{j,k}^{n+1} - \overline{G}_{j-1,k}^{n+1}\right) - \Delta t\, \overline{H}_{j,k}^{n+1}\right] \tag{28}$$

where $z = j\Delta z$, $y = k\Delta y$, $t = n\Delta t$ and $F_{j,k}^{n} = F(U_{j,k}^{n})$, $\overline{F}_{j,k}^{n+1} = F(\overline{U}_{j,k}^{n+1})$, etc.
Note that the spatial derivatives in the predictor step are approximated
by forward difference, while in the corrector step they are approximated
by backward differences. The shear stress and heat flux terms appearing
in F, G, and H are evaluated using backward differences in the predictor
step and forward differences in the corrector step. The net result is
a central difference approximation for the shear stress and heat flux
terms[9].

Using the above finite-difference equations, the computation is
advanced in time from the initial conditions until the "steady-state"

solution is reached. After each computational step, the flow variables are obtained at each interior grid point from the U vector

$$U = \begin{bmatrix} U_1 \\ U_2 \\ U_3 \\ U_4 \end{bmatrix} = [\delta + \delta^2 K(1-\bar{z})] \begin{bmatrix} \rho \\ \rho u \\ \rho v \\ E \end{bmatrix} \tag{29}$$

in the following manner:

$$\rho = U_1 / [\delta + \delta^2 K(1-\bar{z})]$$

$$u = U_2/U_1$$

$$v = U_3/U_1 \tag{30}$$

$$e = U_4/U_1 - \frac{u^2 + v^2}{2}$$

$$p = p(e, \rho)$$

$$T = T(e, \rho)$$

During the present study, the latter two expressions were evaluated using perfect gas relations. However, for the case of air in chemical equilibrium, they could easily be evaluated using the approximate curve fits appearing in Refs. 4 and 5.

Boundary Conditions

The flow conditions at the outer computational boundary in Fig. 7

OUTER
COMPUTATIONAL
BOUNDARY

NK

NK - 1

OUTFLOW
BOUNDARY

INCIDENT
SHOCK

KS

KS - 1 α

BODY

M_∞

2

k = 1
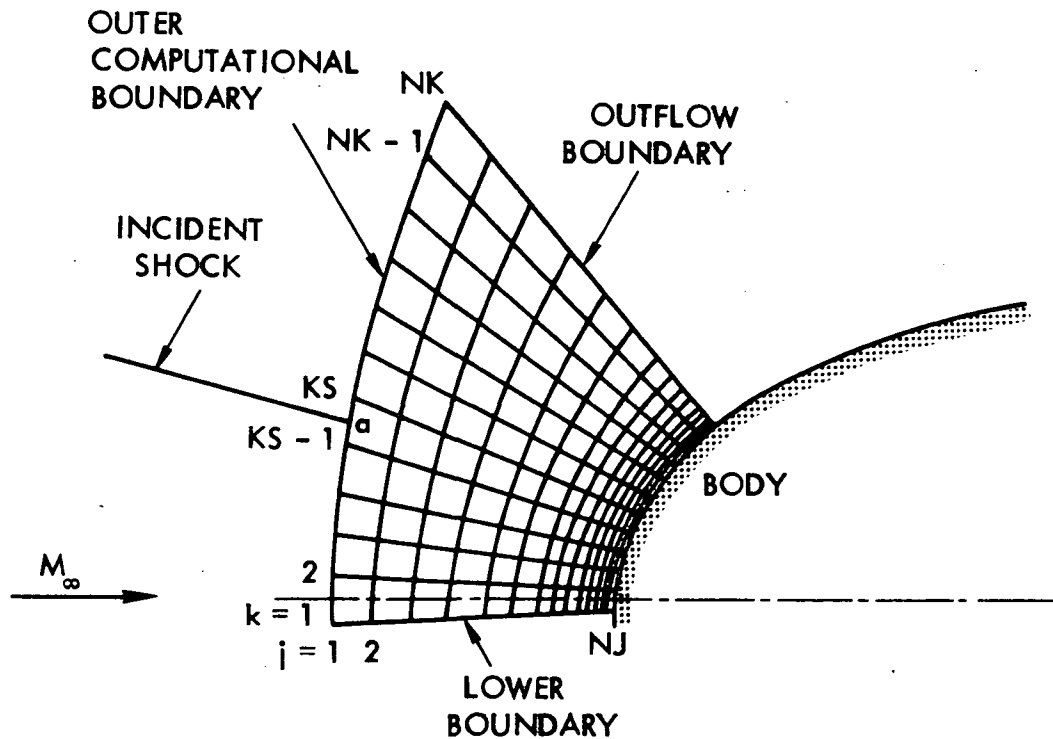
i = 1 2

NJ

LOWER
BOUNDARY

Fig. 7 Computational boundaries

are necessarily different for the "shock-capturing" and "shock-fitting"

methods. For the "shock-capturing" method, freestream conditions are

maintained at all grid points along the outer computational boundary

below the impingement point. For grid points above the impingement point,

the flow variables are set equal to the conditions which exist behind an

oblique shock at the desired shock impingement angle. The impingement

point is placed, for simplicity, halfway between any two adjacent grid

points along the outer computational boundary.

When the "shock-fitting" method is employed, the flow conditions

at the outer computational boundary are those conditions which exist

immediately downstream of the bow shock as determined by the Rankine-

Hugoniot relations. Consequently, it is necessary to include logic

which will permit this boundary to move with the bow shock as the latter moves toward its "steady-state" position. The approach used here is somewhat similar to the approach previously used by Thomas, et al.[10] and Kutler, et al.[11] in their inviscid steady flow computations. Their predictor-corrector approach has been modified for the present unsteady computations.

The coordinate system used for the "shock-fitting" procedure is shown in Fig. 8. The local velocity of the shock is given
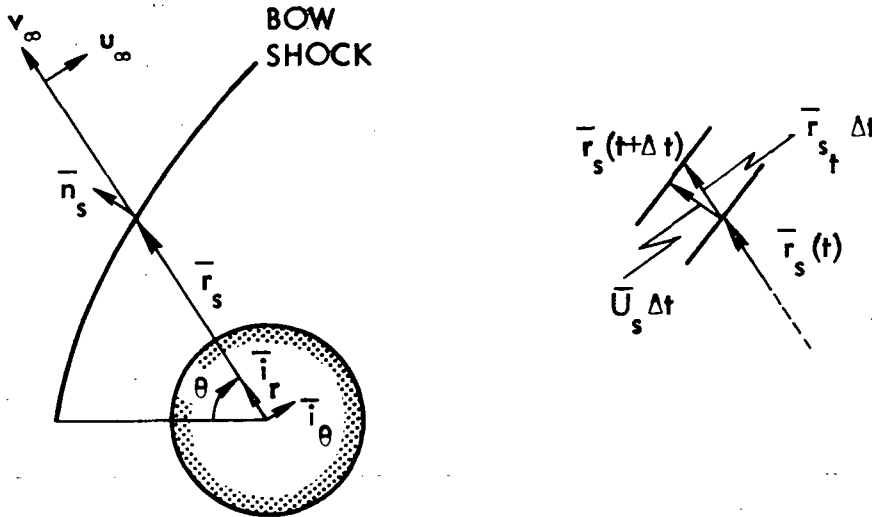

Fig. 8 Notation for "shock-fitting" procedure.

by

$$\bar{U}_s = U_s \, \bar{n}_s \tag{31}$$

where $\bar{n}_s$ denotes the outward unit normal to the shock given by

$$\bar{n}_s = \frac{\bar{i}_r - \left(r_{s_\theta}/r_s\right)\bar{i}_\theta}{[1 + (r_{s_\theta}/r_s)^2]^{\frac{1}{2}}} \tag{32}$$

The magnitude of the local shock velocity can be related to the radial shock velocity (r_{s_t}) by

$$U_s = \bar{r}_{s_t} \cdot \bar{n}_s \tag{33}$$

or

$$U_s = \frac{r_{s_t}}{[1 + (r_{s_\theta}/r_s)^2]^{\frac{1}{2}}} \tag{34}$$

The vector component of the fluid velocity normal to and measured with respect to the moving shock is given by

$$\bar{V}_1 = [(\bar{q}_\infty - \bar{U}_s) \cdot \bar{n}_s]\bar{n}_s \tag{35}$$

where $\bar{q}_\infty = v_\infty\bar{i}_r + u_\infty\bar{i}_\theta$. When Eqs. (32) and (34) are substituted into Eq. (35), the following expression is obtained for the magnitude of $\bar{V}_1$

$$V_1 = \frac{r_{s_t} - v_\infty + u_\infty(r_{s_\theta}/r_s)}{[1 + (r_{s_\theta}/r_s)^2]^{\frac{1}{2}}} \tag{36}$$

from which r_{s_t} can be obtained as

$$r_{s_t} = V_1 [1 + (r_{s_\theta}/r_s)^2]^{\frac{1}{2}} + v_\infty - u_\infty (r_{s_\theta}/r_s) \tag{37}$$

The above equations are used in the "shock-fitting" method in the following manner. First, the shock wave radial distance is evaluated by use of the Euler predictor

$$\overline{r_{s_k}^{n+1}} = r_{s_k}^n + \Delta t \, r_{s_{t_k}}^n \qquad (2 \le k \le NK-1) \tag{38}$$

using Eq. (37) to evaluate $r_{s_{t_k}}^n$. The derivative $r_{s_{\theta_k}}^n$ which appears in Eq. (37) is evaluated using the second-order central difference formula

$$r_{s_{\theta_k}}^n = (r_{s_{k+1}}^n - r_{s_{k-1}}^n)/2\Delta\theta \tag{39}$$

For the grid points immediately above (k = KS) and below (k = KS - 1) the shock impingement point, it is not acceptable to use Eq. (39) because of the discontinuity in the shock slope at the impingement point. Instead, the derivatives at k = KS and k = KS - 1 are evaluated using the second-order expressions

$$r_{s_{\theta_{KS}}}^n = \left(3r_{s_{KS}}^n - 4r_{s_a}^n + r_{s_{KS+1}}^n\right)/3\Delta\theta$$

$$r_{s_{\theta_{KS-1}}}^n = \left(4r_{s_a}^n - 3r_{s_{KS-1}}^n - r_{s_{KS-2}}^n\right)/3\Delta\theta \tag{40}$$

where the radial distance to the shock impingement point (r_{s_a}) is determined in the predictor step using a second-order extrapolation given by

$$r_{s_a}^n = \left(15 \, r_{s_{KS}}^n - 10 \, r_{s_{KS+1}}^n + 3 \, r_{s_{KS+2}}^n\right)/8 \tag{41}$$

Eqs. (40) and (41) were derived by assuming that the impingement point (a) is halfway between the grid points KS-1 and KS.

The next step is to compute the pressures $\overline{P_{1,k}^{n+1}}$ immediately behind the bow shock using the modified MacCormack scheme

$$\overline{U_{1,k}^{n+1}} = U_{1,k}^n - \frac{\Delta t}{\Delta y}\left(F_{1,k+1}^n - F_{1,k}^n\right) - \frac{\Delta t}{\Delta z}\left(G_{2,k}^n - G_{1,k}^n\right) - \Delta t \, H_{1,k}^n \tag{42}$$

Once the pressures behind the bow shock are computed, $\overline{V_{1_k}^{n+1}}$ and $\overline{\rho_{1,k}^{n+1}}$ can be computed using the normal shock relations

$$\overline{V_{1_k}^{n+1}} = \left[\left(\frac{\gamma-1}{2}\right)\frac{P_\infty}{\rho_\infty}\left[\frac{\overline{P_{1,k}^{n+1}}}{P_\infty} + \frac{\gamma-1}{\gamma+1}\right]\right]^{\frac{1}{2}} \tag{43}$$

$$\overline{\rho_{1,k}^{n+1}} = \rho_\infty \frac{\dfrac{\overline{P_{1,k}^{n+1}}}{P_\infty} + \dfrac{\gamma-1}{\gamma+1}}{1 + \left(\dfrac{\gamma-1}{\gamma+1}\right)\dfrac{\overline{P_{1,k}^{n+1}}}{P_\infty}} \tag{44}$$

The components of the fluid velocity behind the bow shock are evaluated using relative velocity equations which give

$$u^{\overline{n+1}}_{1,k} = u_\infty - \left(1 - \frac{\rho_\infty}{\rho^{\overline{n+1}}_{1,k}}\right) \frac{\left[r^{\overline{n+1}}_{s_{t_k}} - v_\infty + u_\infty\left(r^{\overline{n+1}}_{s_{\theta_k}}/r^{\overline{n+1}}_{s_k}\right)\right]\left(r^{\overline{n+1}}_{s_{\theta_k}}/r^{\overline{n+1}}_{s_k}\right)}{\left[1 + \left(r^{\overline{n+1}}_{s_{\theta_k}}/r^{\overline{n+1}}_{s_k}\right)^2\right]}$$

(45)

$$v^{\overline{n+1}}_{1,k} = v_\infty + \left(1 - \frac{\rho_\infty}{\rho^{\overline{n+1}}_{1,k}}\right) \frac{\left[r^{\overline{n+1}}_{s_{t_k}} - v_\infty + u_\infty\left(r^{\overline{n+1}}_{s_{\theta_k}}/r^{\overline{n+1}}_{s_k}\right)\right]}{\left[1 + \left(r^{\overline{n+1}}_{s_{\theta_k}}/r^{\overline{n+1}}_{s_k}\right)^2\right]}$$

where $r^{\overline{n+1}}_{s_{t_k}}$ is obtained from Eq. (37). The remaining unknown $T^{\overline{n+1}}_{1,k}$ is

calculated using the state relationship $T = T(e,\rho)$. This completes the

predictor step. The corrector step is identical to the predictor step

except that the shock wave radial distance is evaluated using the modified

Euler corrector

$$r^{n+1}_{s_k} = r^n_{s_k} + \frac{\Delta t}{2}\left(r^n_{s_{t_k}} + r^{\overline{n+1}}_{s_{t_k}}\right)$$

(46)

and Eqs. (41) and (42) are replaced by

$$r^{\overline{n+1}}_{s_a} = \left(15\, r^{\overline{n+1}}_{s_{KS-1}} - 10\, r^{\overline{n+1}}_{s_{KS-2}} + 3\, r^{\overline{n+1}}_{s_{KS-3}}\right)/8$$

(47)

and

$$U^{n+1}_{1,k} = \frac{1}{2}\left[U^n_{1,k} + U^{\overline{n+1}}_{1,k} - \frac{\Delta t}{\Delta y}\left(F^{\overline{n+1}}_{1,k} - F^{\overline{n+1}}_{1,k-1}\right) - \frac{\Delta t}{\Delta z}\left(G^{\overline{n+1}}_{2,k} - G^{\overline{n+1}}_{1,k}\right) - \Delta t\, H^{\overline{n+1}}_{1,k}\right]$$

(48)

In addition, the "predicted" variables $\overline{(n+1)}$ in Eqs. (43), (44), and (45) are replaced by "corrected" variables (n+1) during the corrector step.

The calculation of the boundary conditions using the "shock-fitting" method described above is performed before the predictor or corrector steps are initiated at interior grid points. All other boundary conditions are calculated after the predictor or corrector step is completed at interior grid points. The flow conditions along the outflow boundary in Fig. 7 are determined using a second-order extrapolation of interior grid point data. For example, the pressure is obtained from

$$P_{j,NK} = 3P_{j,NK-1} - 3P_{j,NK-2} + P_{j,NK-3} \tag{49}$$

Along the body surface, the following conditions are imposed

$$P_{k,NJ} = P_{k,NJ-1}$$

$$T_{k,NJ} = T_w$$

$$\rho_{k,NJ} = P_{k,NJ}/RT_{k,NJ} \tag{50.}$$

$$u_{k,NJ} = 0$$

$$v_{k,NJ} = 0$$

During some early computations, a different set of boundary conditions was used at the body surface. In these computations the density at the body surface was determined using a second-order extrapolation normal to the body and the pressure was found from the equation of state. These boundary conditions proved to be unstable, however, when applied to cases

where the body was highly cooled, while Eq. (50) gave stable results.

The flow conditions along the lower boundary in Fig. 7 are determined using either simple reflection about an axis of symmetry which is placed midway between the k = 1 and k = 2 rows of grid points or a second-order extrapolation of interior grid point data for the case of supersonic outflow conditions.

Initial Conditions

In all computations performed thus far, the blunt body flow without the impinging shock was computed first. The initial conditions for this calculation are obtained by using an approximate curve fit for the location and shape of the bow shock along with a Newtonian pressure distribution at the body. The approximate curve fit of Billig[12] is used to find r_s and r_{s_θ} along the shock. Eqs. (36), (43), (44), and (45) are then used (with r_{s_t} set equal to zero) to find the initial conditions immediately behind the shock. The initial flow conditions at the wall are obtained using the known wall temperature in conjunction with the pressures from the Newtonian pressure distribution. The densities at the wall are obtained from the equation of state and the velocities are set equal to zero. The initial flow conditions at interior grid points are obtained by assuming a linear variation between the flow conditions immediately behind the bow shock and the wall conditions.

After a "steady-state" solution is achieved for the undisturbed blunt body flow, the impinging shock is introduced by resetting the free-stream flow variables above the impingement point equal to the values

which exist behind the desired oblique impinging shock. The computation is then carried to a new "steady-state".

Stability

Since the present computational method is explicit, the maximum time increment (Δt) must be limited to ensure stability. For high Reynolds number flows, the maximum time increment is determined from the usual C.F.L. condition[8]. For low Reynolds number flows, the following equation derived by Li[13] can be used:

$$\Delta t \leq \frac{\rho(\Delta\eta)^2}{8\mu}$$

(51)

NUMERICAL RESULTS

The computational methods developed in this study have been applied
to several 2-D viscous, blunt body flows with an impinging shock. Both
the "shock-capturing" and "shock-fitting" methods have been used.

Case I. ("Shock-Capturing" method)

The first test case consists of nitrogen flowing over a circular
cylinder at low Reynolds number. The flow conditions for this case
are

$$M_\infty = 4.2 \qquad\qquad p_\infty = .0735 \text{ newtons/m}^2$$

$$Re_{D_\infty} = 200 \qquad\qquad T_\infty = 96.1 \text{ }^\circ K$$

$$\text{(52)}$$

$$Pr = .687 \qquad\qquad D = .6096 \text{ m}$$

$$\gamma = 1.4 \qquad\qquad T_w = T_{t_\infty} = 435.2 \text{ }^\circ K$$

The "shock-capturing" method is ideally suited for this computation since
the bow shock is relatively thick for low values of Reynolds number. For
this case, the outer computational boundary was a circle with a radius
equal to the diameter of the cylinder. The lower boundary (k=1) was
located along a ray 1° below the undisturbed stagnation streamline and
the outflow boundary (k=NK) was located along a ray 39.1° above the
undisturbed stagnation streamline. A mesh consisting of 21 equally
spaced grid points in both the y and z directions was used in this
computation.

Initially, the blunt body flow without the impinging shock was computed using freestream initial conditions at all grid points. This computation took 1425 time steps to reach a "steady-state" and used approximately 24.2 minutes of CPU time on the IBM 360-65 computer. The results of this computation are seen in the contour plots of Figs. 9, 10, and 11 which show lines of constant Mesh number, temperature, and pressure, respectively. The finite thickness of the bow shock is evident in these figures.

The variation of the computed temperature along the stagnation streamline is shown in Fig. 12, along with the experimentally measured wire temperatures of Ref. 14. Although the wire temperatures cannot be compared directly with the computed static temperatures, they can be used to indicate the location of the bow shock. The wire temperatures have been normalized so that their values in the freestream and at the body agree with the computed static pressures at these points. The location of the bow shock in the present computation falls between the experimentally determined locations in Fig. 12. This is the desired result, since the present flow conditions are between the flow conditions of the two experimental tests of Ref. 14.

An impinging shock was then introduced into the "steady-state" blunt body computation along a ray 20° above the stagnation streamline of the undisturbed flow field. This was accomplished by resetting the freestream flow variables, along the outer computational boundary above the impingement point, equal to the values which exist behind a 20° shock. The ratio of the pressures across this impinging shock was $p_{2_{\infty}}/p_{1_{\infty}} = 2.24$.
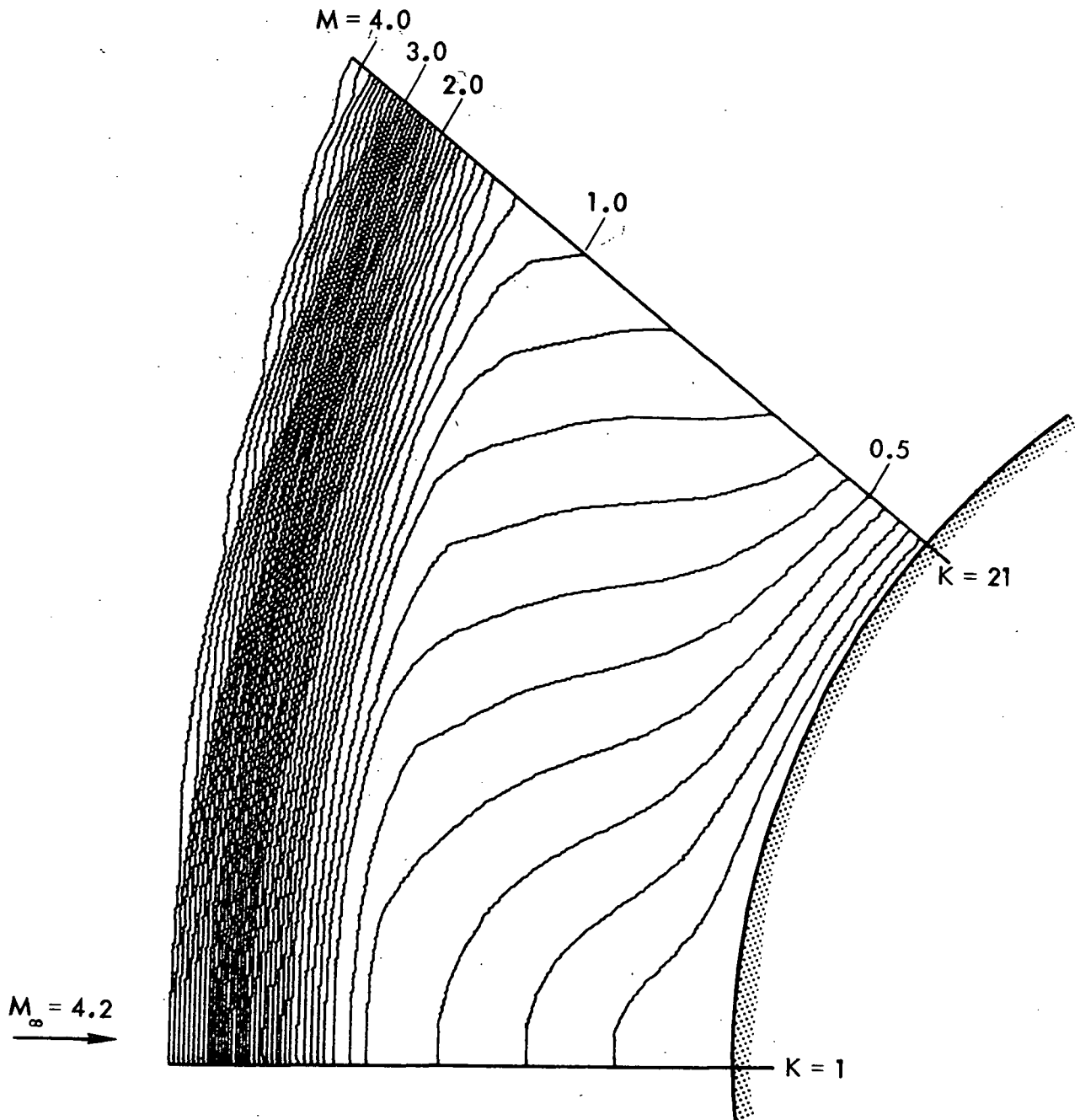
Fig. 9.   Constant Mach number lines,
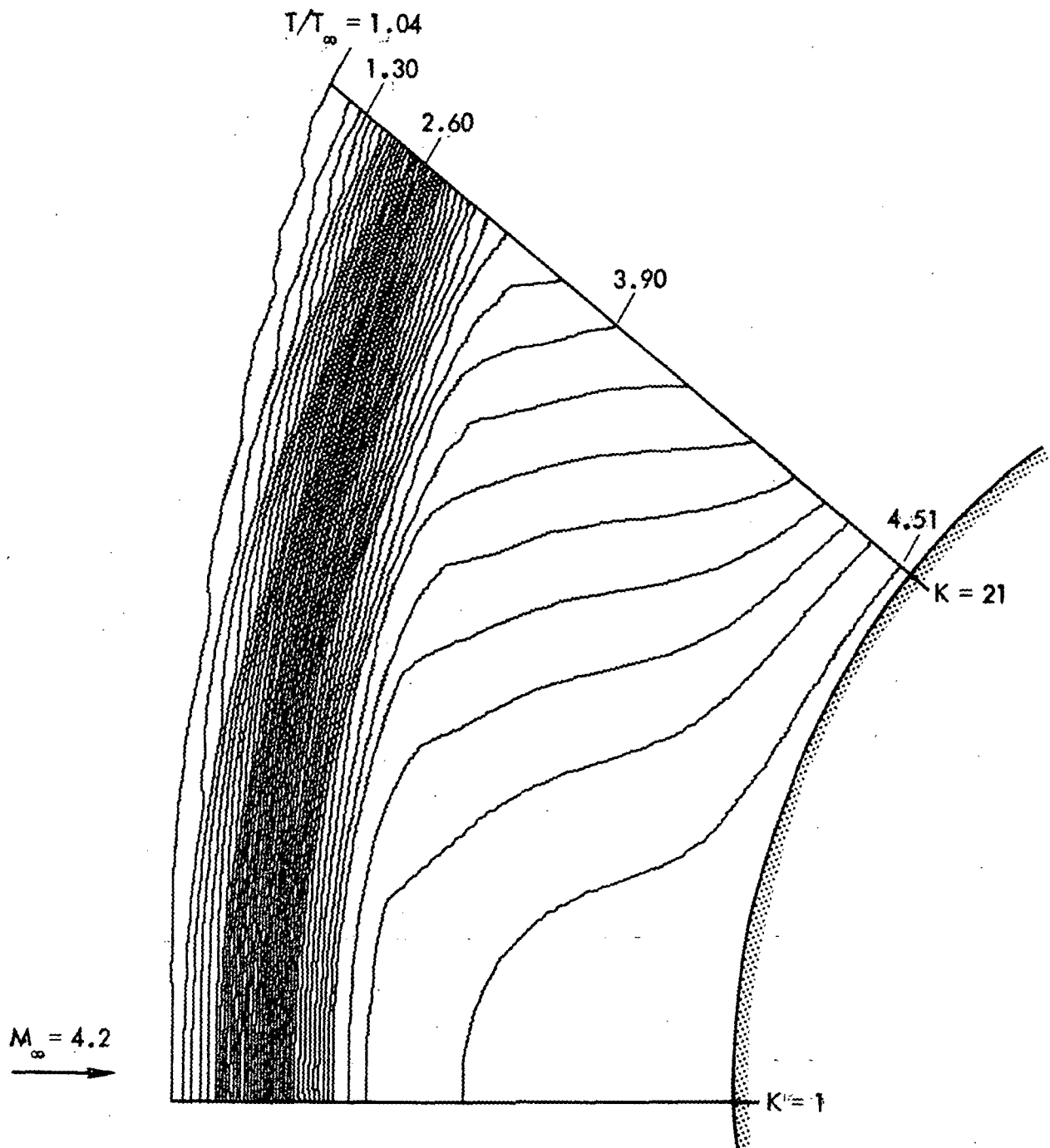   Case I (no impingement).

Fig. 10. Constant temperature lines,
Case I (no impingement).

$M_\infty = 4.2$

$p/p_\infty = 2.6 \quad 7.8 \quad 13.0 \quad 18.2 \qquad 20.8$
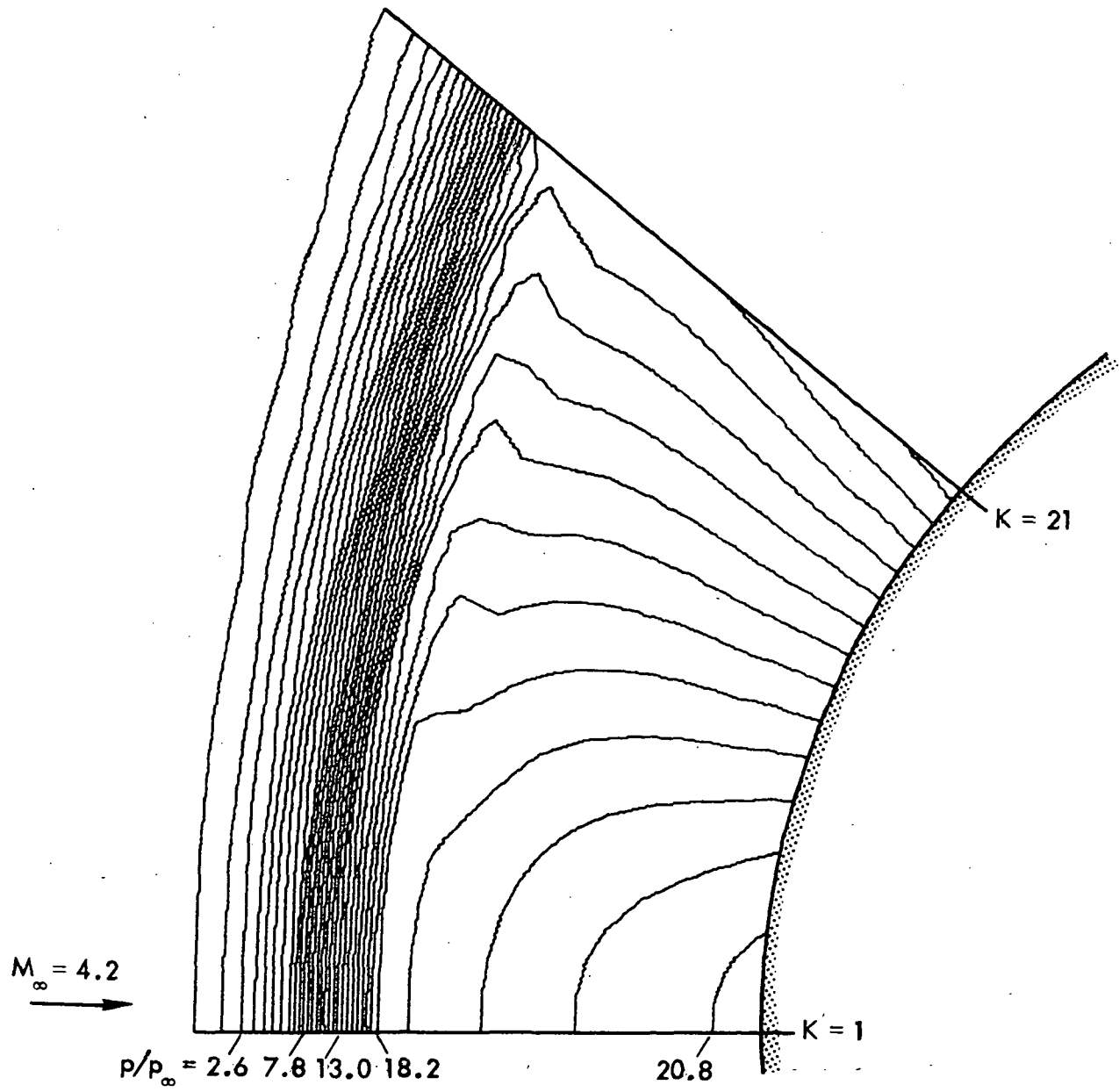
K = 21

K = 1

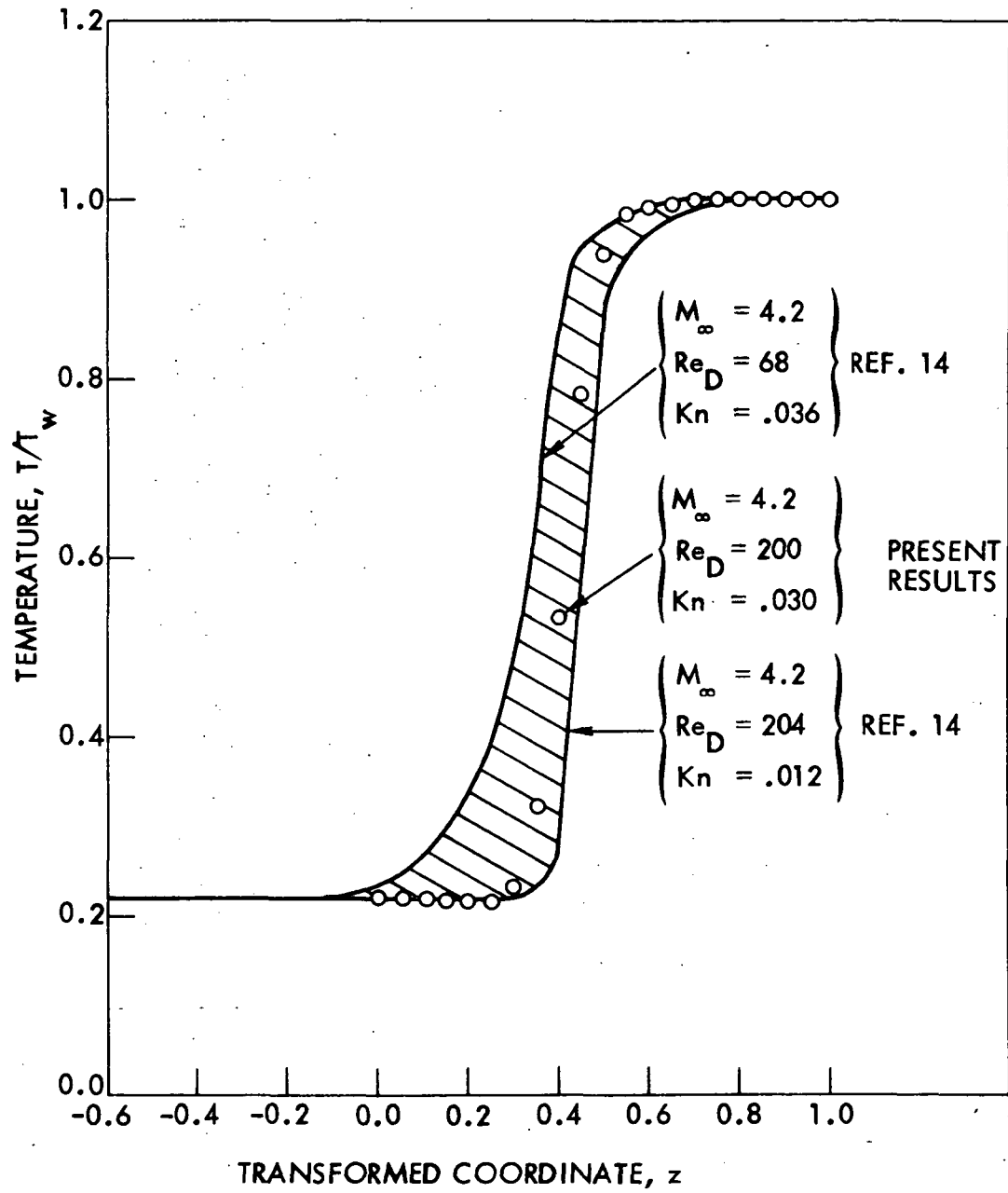Fig. 11.   Constant pressure lines,
Case I (no impingement).

Fig. 12. Variation of temperature along
stagnation streamline.

The computation was then carried to a new "steady-state" which took an additional 2325 steps and used approximately 39.5 minutes of CPU time on the IBM 360-65 computer. The results of this computation are shown in the contour plots of Figs. 13, 14, and 15. The large effect of the
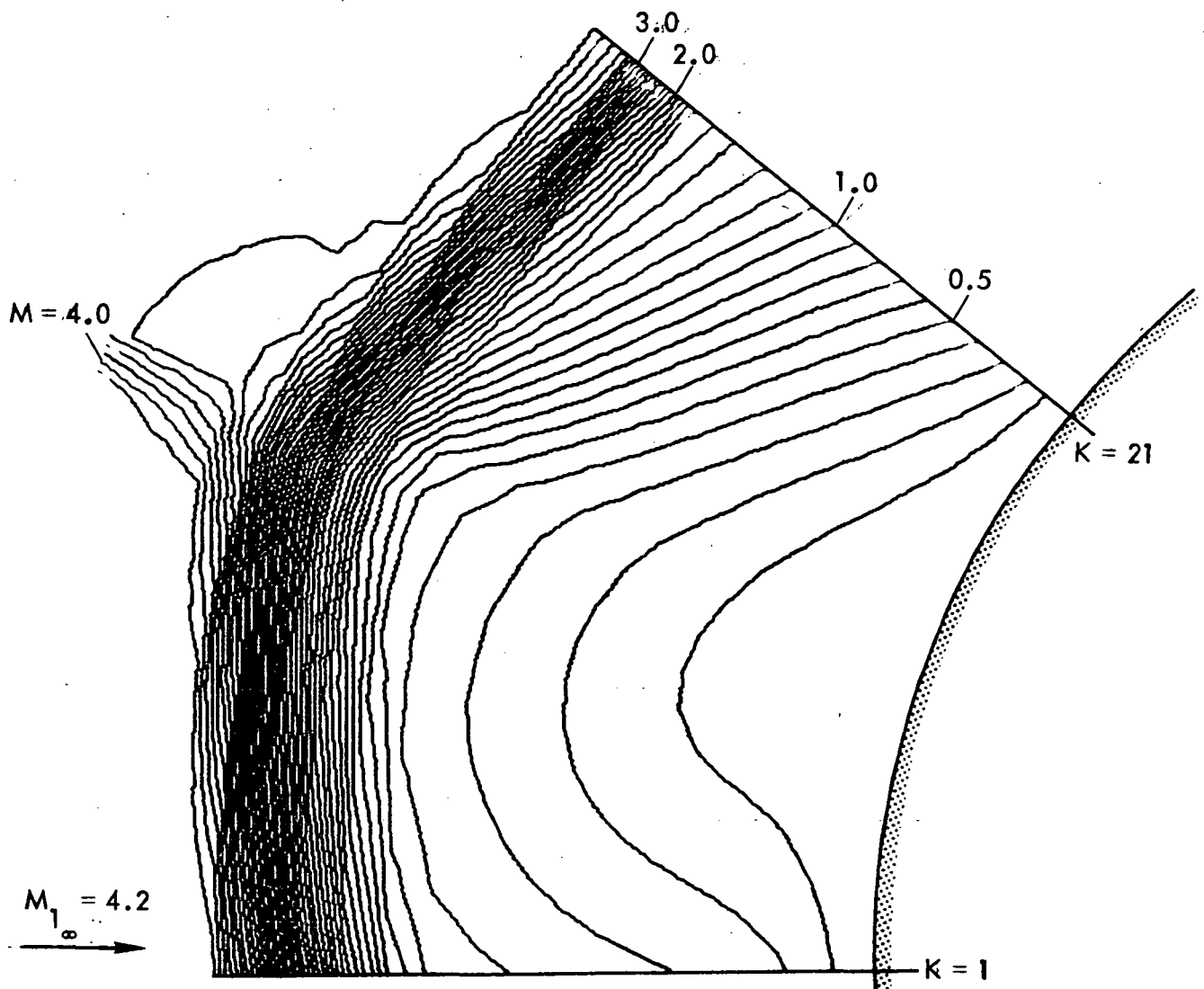
Fig. 13. Constant Mach number lines, Case I (20° shock impingement).
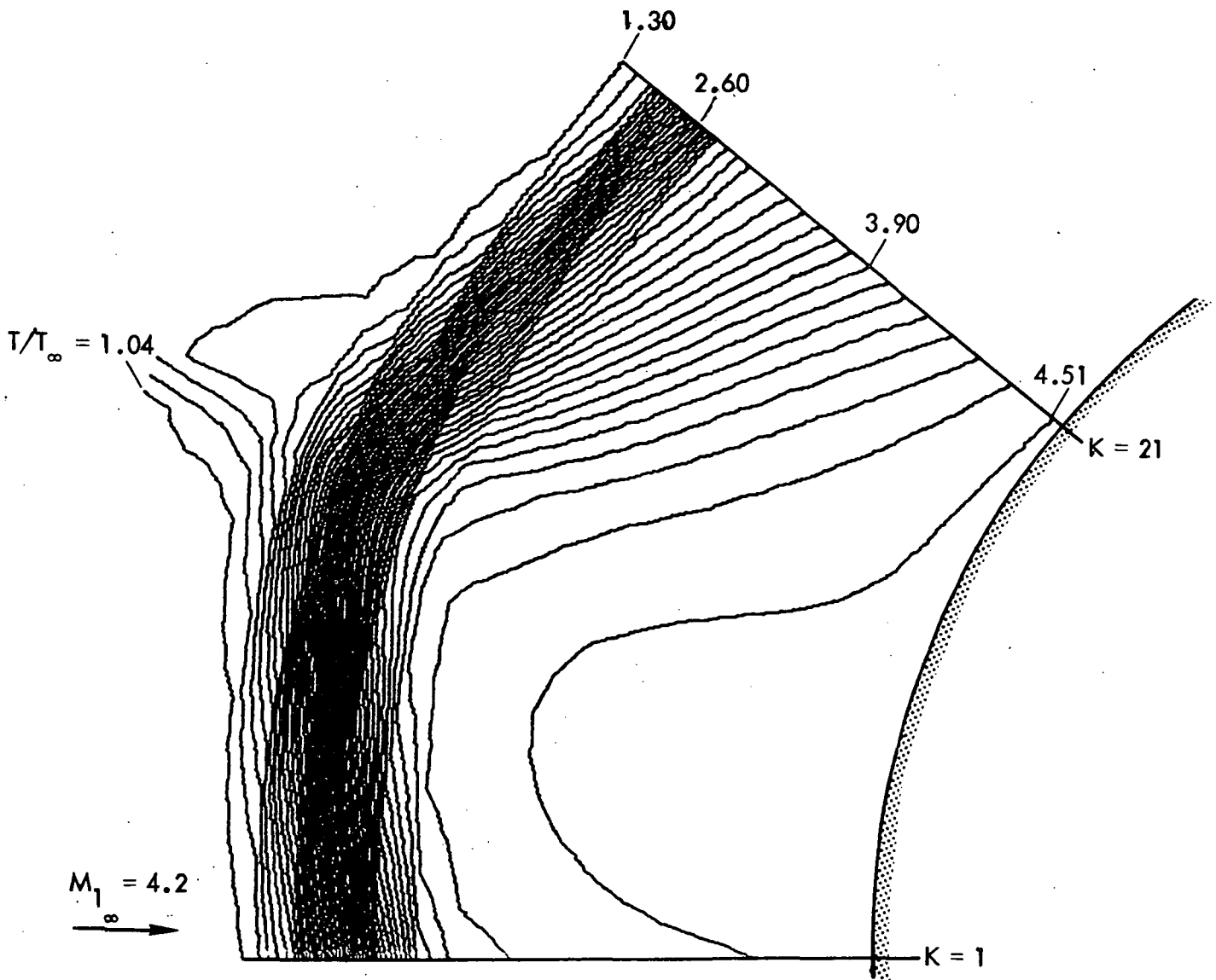
Fig. 14. Constant temperature lines, Case I .
(20° shock impingement).

incident shock on the undisturbed flow field is evident when these

figures are compared with the previous contour plots. Comparisons of

the surface pressures and heat transfers between the undisturbed

computation and the present shock impingement computation are shown

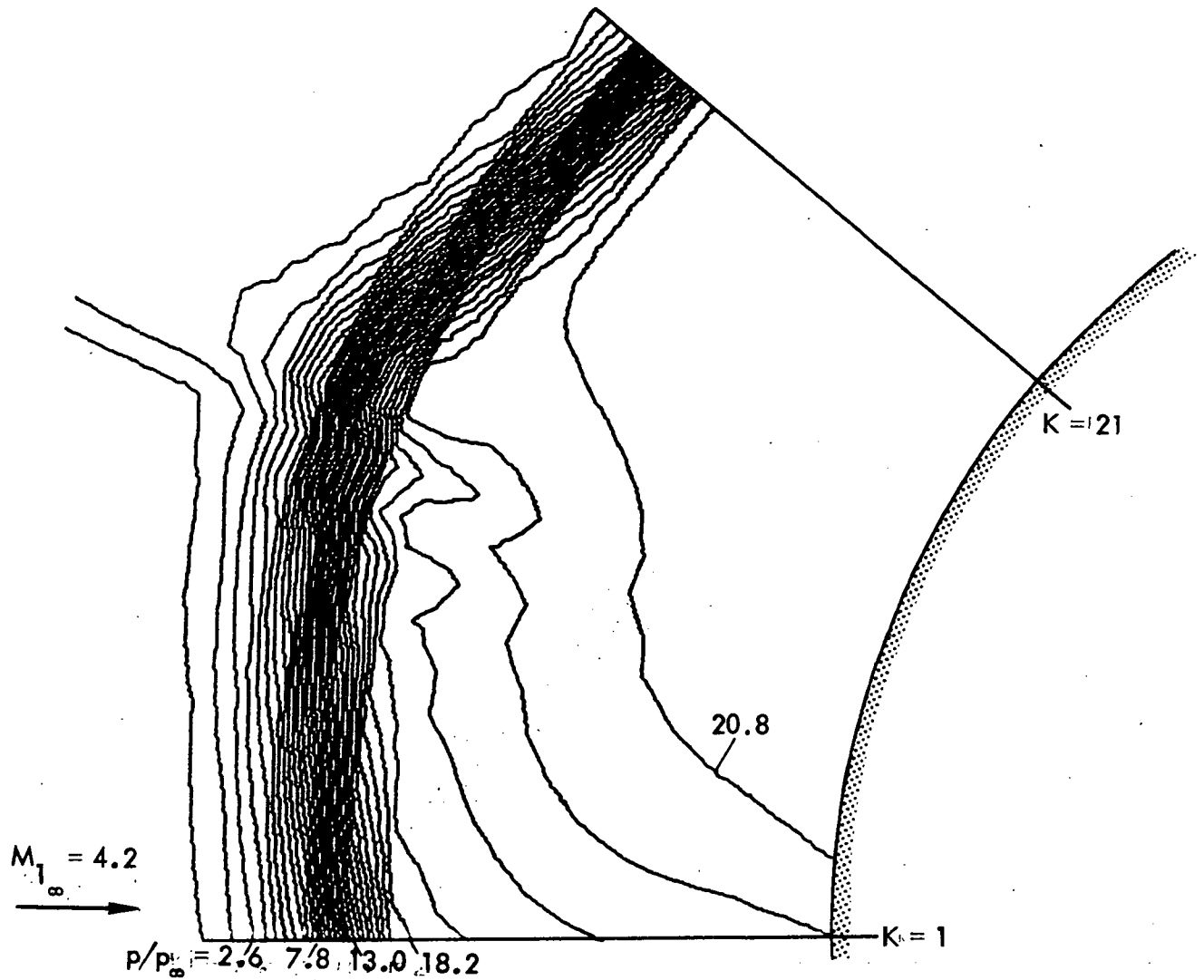in Figs. 16 and 17. The incident shock causes an increase in wall

Fig. 15. Constant pressure lines, Case I .
(20° shock impingement).

pressure of 72% and an increase in heat transfer of 49% over the un-

disturbed values at the point where the outflow boundary (k=21) inter-
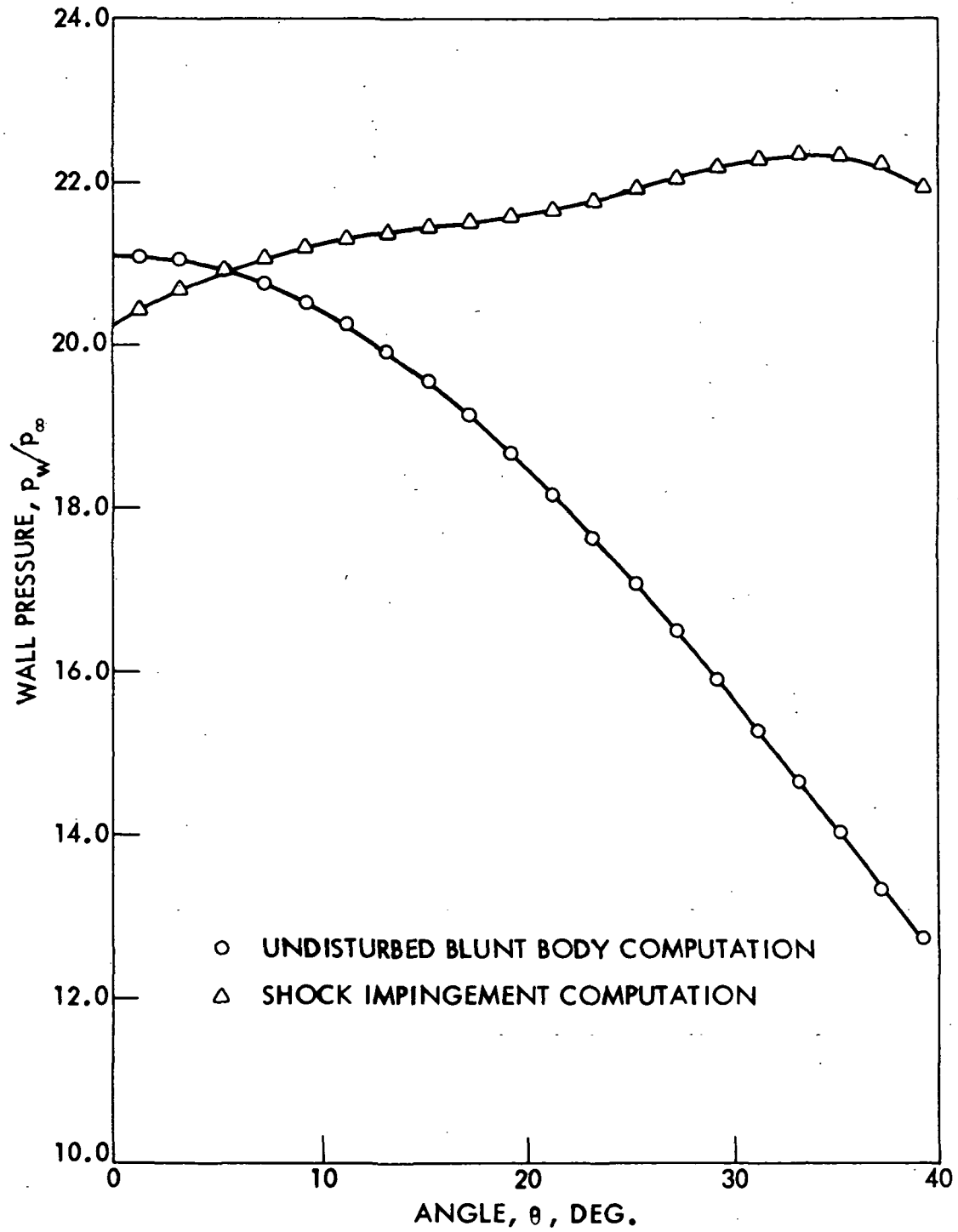
sects the body.

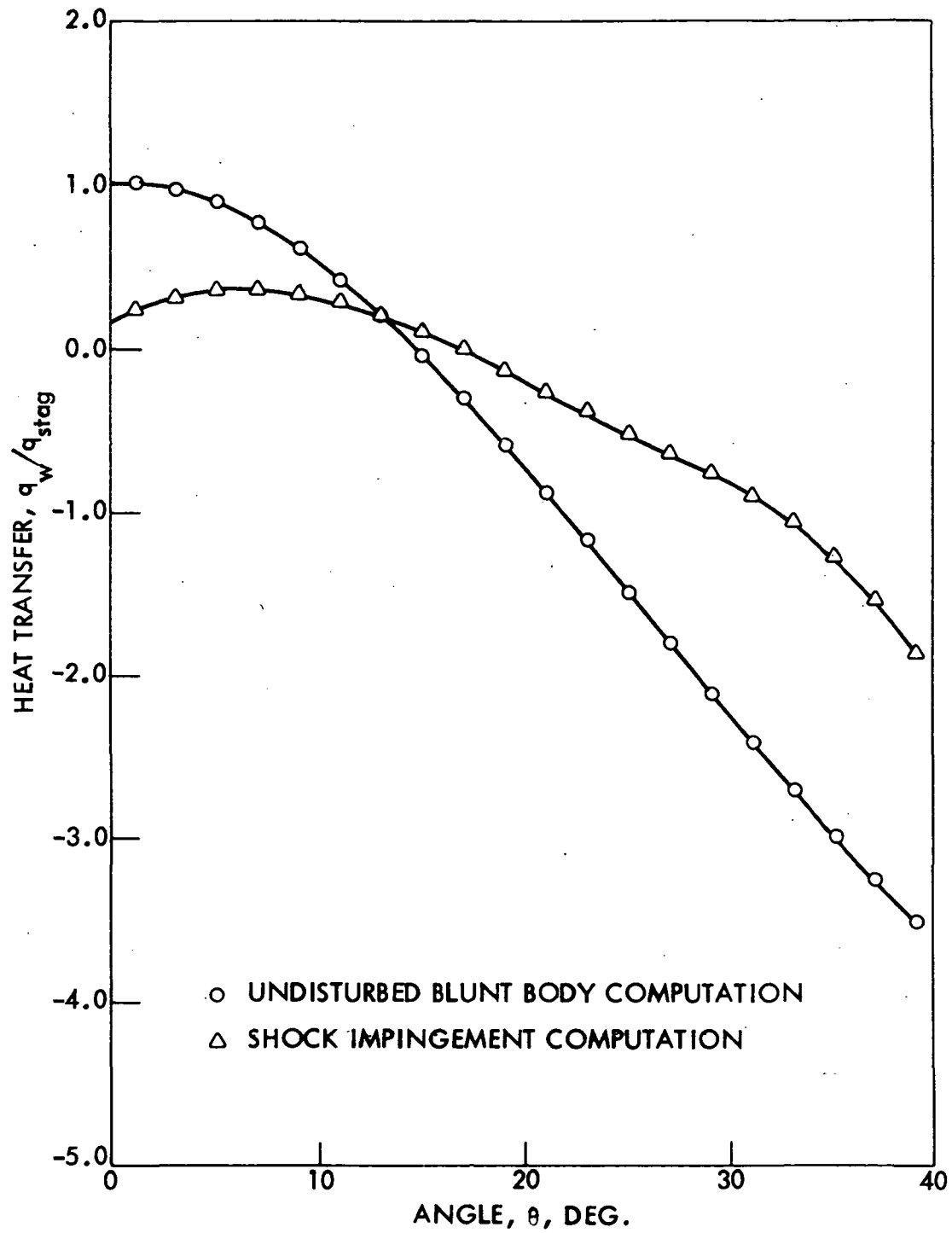Fig. 16.   Comparison of wall pressures.

Fig. 17. Comparison of heat transfers.

Case II. ("Shock-Fitting" Method)

This test case consists of air flowing over a circular cylinder with the following conditions

M_∞ = 12.145 P_∞ = 19.8 newtons/m^2

Re_{D_∞} = 19,838 T_∞ = 254 $^\circ$K

Pr = .72   D = .3048 m

γ = 1.4 T_w = 1445 $^\circ$K

These flow conditions are identical to those that will exist normal to the leading edge of the Orbiter wing (sweep angle of 45°) at 61 km (200,000 ft).

The "shock-fitting" method was used for this computation since the moderately high Reynolds number causes the bow shock to be relatively thin. A mesh consisting of 51 equally spaced grid points in the y direction and 31 equally spaced grid points in the z direction was used. The lower outflow boundary (k=1) was located along a ray 61.5° below the undisturbed stagnation streamline while the upper outflow boundary was located along a ray 88.5° above the undisturbed stagnation streamline. These boundaries were placed so that the flow passing out of each of them was supersonic everywhere except in the boundary layer.

As before, the blunt body flow without the impinging shock was computed initially. The results of this computation for $\beta=0$ are shown in the contour plots of Figs. 18, 19, and 20. Only the results from k=21 to k=51

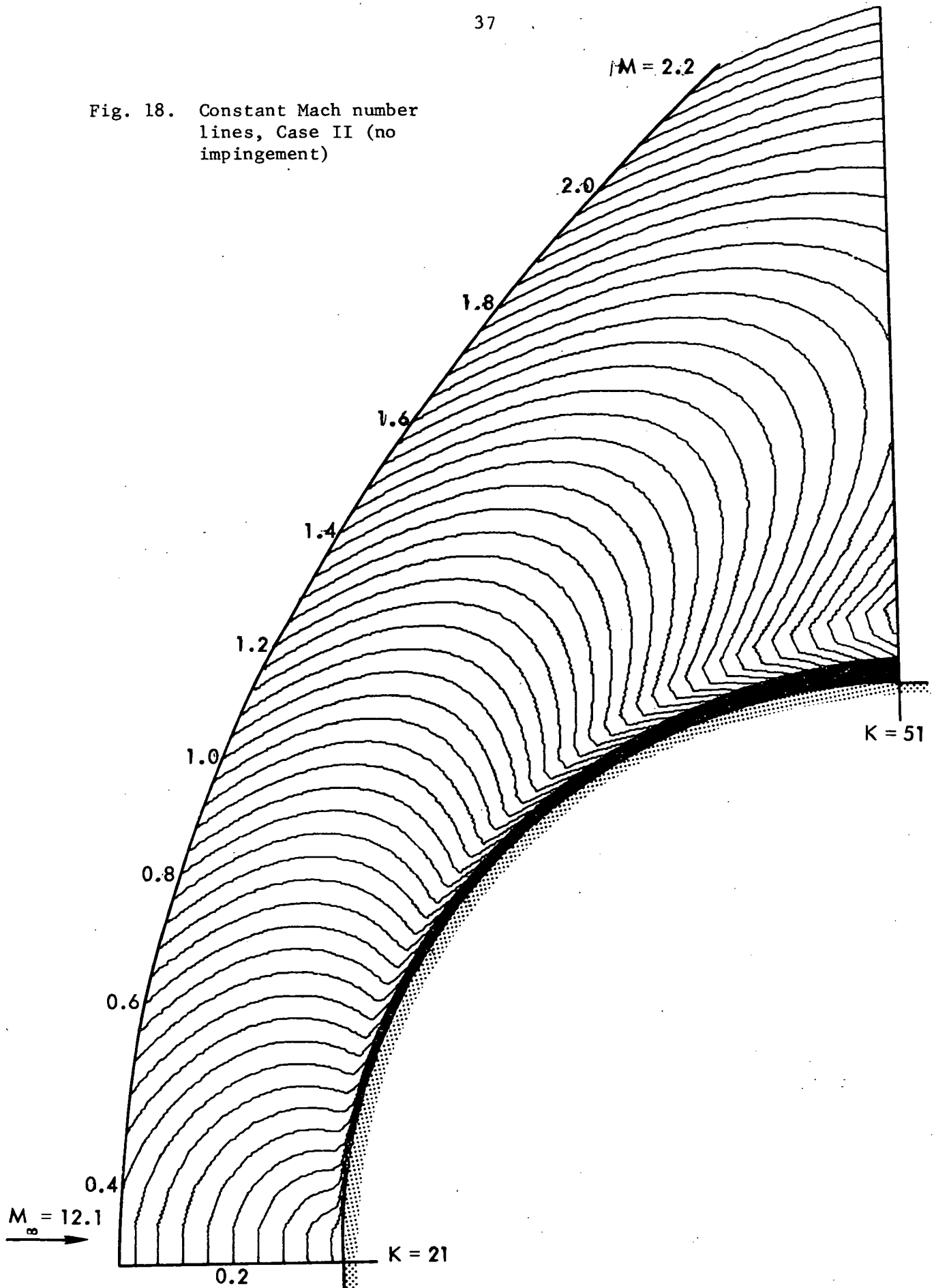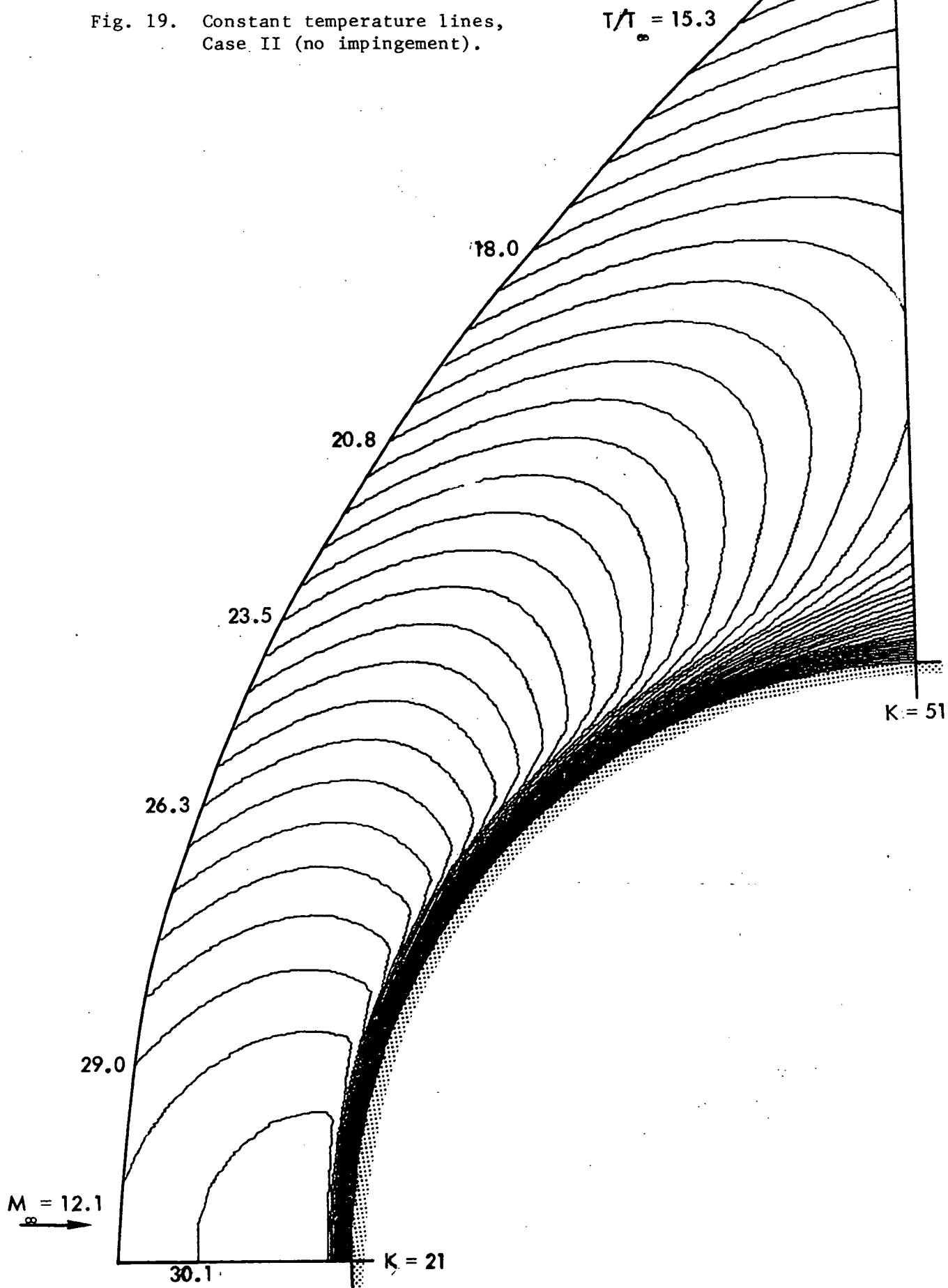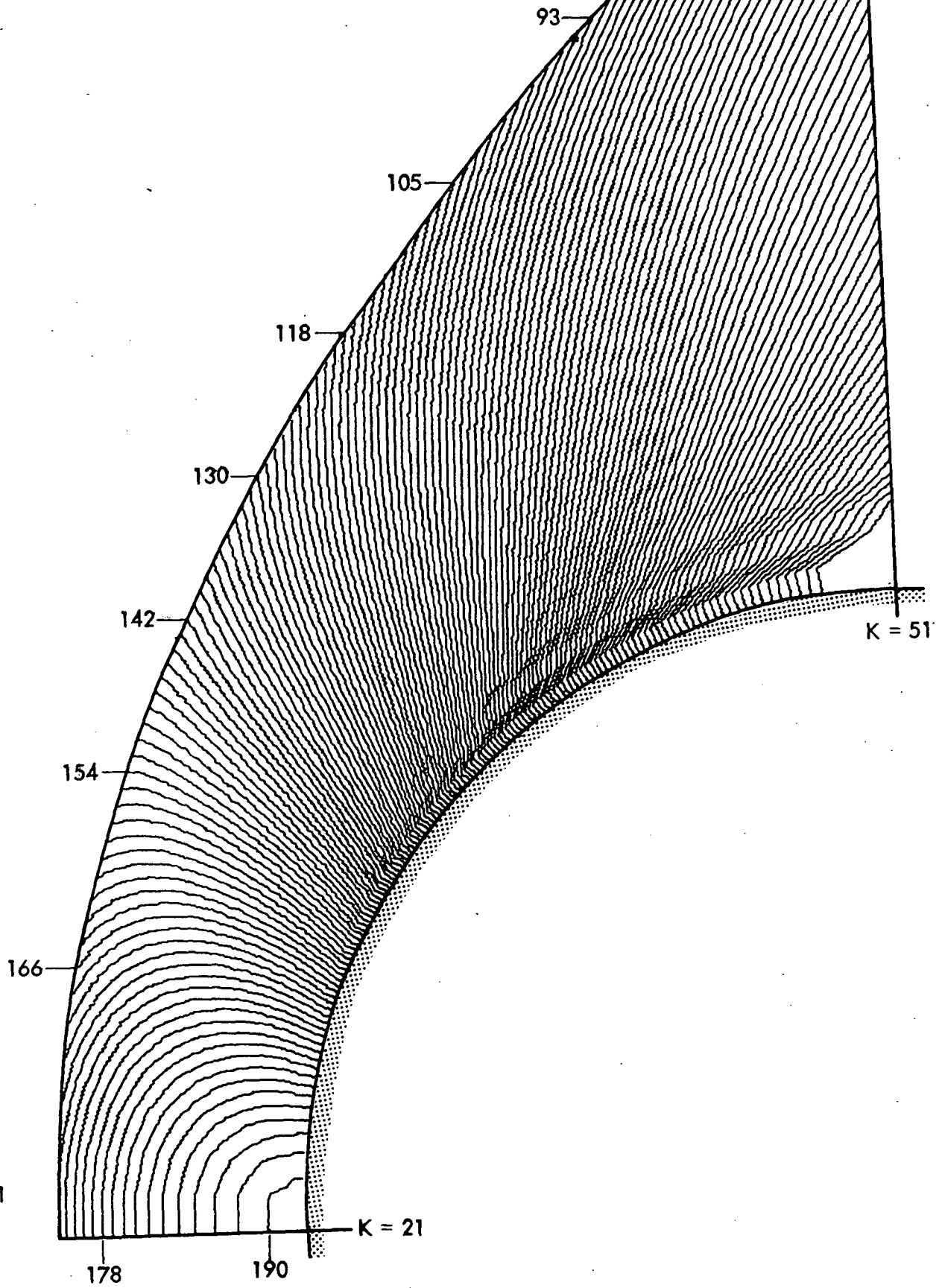Fig. 18. Constant Mach number lines, Case II (no impingement)

$M = 2.2$

2.0

1.8

1.6

1.4

1.2

1.0

0.8

0.6

0.4

$M_\infty = 12.1$

0.2

K = 21

K = 51

Fig. 19. Constant temperature lines,
Case II (no impingement).

$T/T_\infty = 15.3$

18.0

20.8

23.5

26.3

29.0

$M_\infty = 12.1$

30.1

$K = 21$

$K = 51$

Fig. 20. Constant pressure lines,
Case II (no impingement).

$p/p_\infty = 81$

93

105

118

130

142

K = 51

154

166

K = 21

178

190

$M_\infty = 12.1$

are plotted. The stagnation streamline is located halfway between k=21

and k=22. The boundary layer is clearly evident in these figures. This

undisturbed computation was repeated using both the exponential stretching

(Eq. (16), with β = 3) and the logarithmic stretching (Eq. (A1), with

β' = 1.2 and α = 0). A comparison of the temperature profiles at the

stagnation point for the three different computations is shown in Fig. 21.

Included in this figure is the temperature profile computed by the

BLIMP[15] boundary layer program, assuming a perfect gas. Excellent agree-

ment is achieved for all computations. Comparisons of the temperature

and density profiles at various points around the cylinder for the

logarithmic stretching case are shown in Figs. 22 and 23. Again, the

agreement between the present results and the BLIMP program results is

very good.

An impinging shock wave was then introduced into the previous "steady-

state" undisturbed computation. This relatively weak shock wave was

inclined to the freestream at an angle of $5\frac{1}{2}^{\circ}$ and impinged on the bow

shock at θ = 39° (halfway between k=34 and k=35 along j=1). The ratio

of the pressures across this impinging shock was $p_{2_\infty}/p_{1_\infty}$ = 1.42. The

computation was then carried to a new "steady-state" and the resulting

contour plots for β = 0 are shown in Figs. 24, 25, and 26. These

figures clearly show the shear layer which originates from the impingement

point and passes out the upper outflow boundary. This shock interaction

pattern corresponds to Edney's Type III. The effect of the impinging

shock on the shape of the bow shock is shown in Fig. 27.

When the present shock impingement case was recomputed using

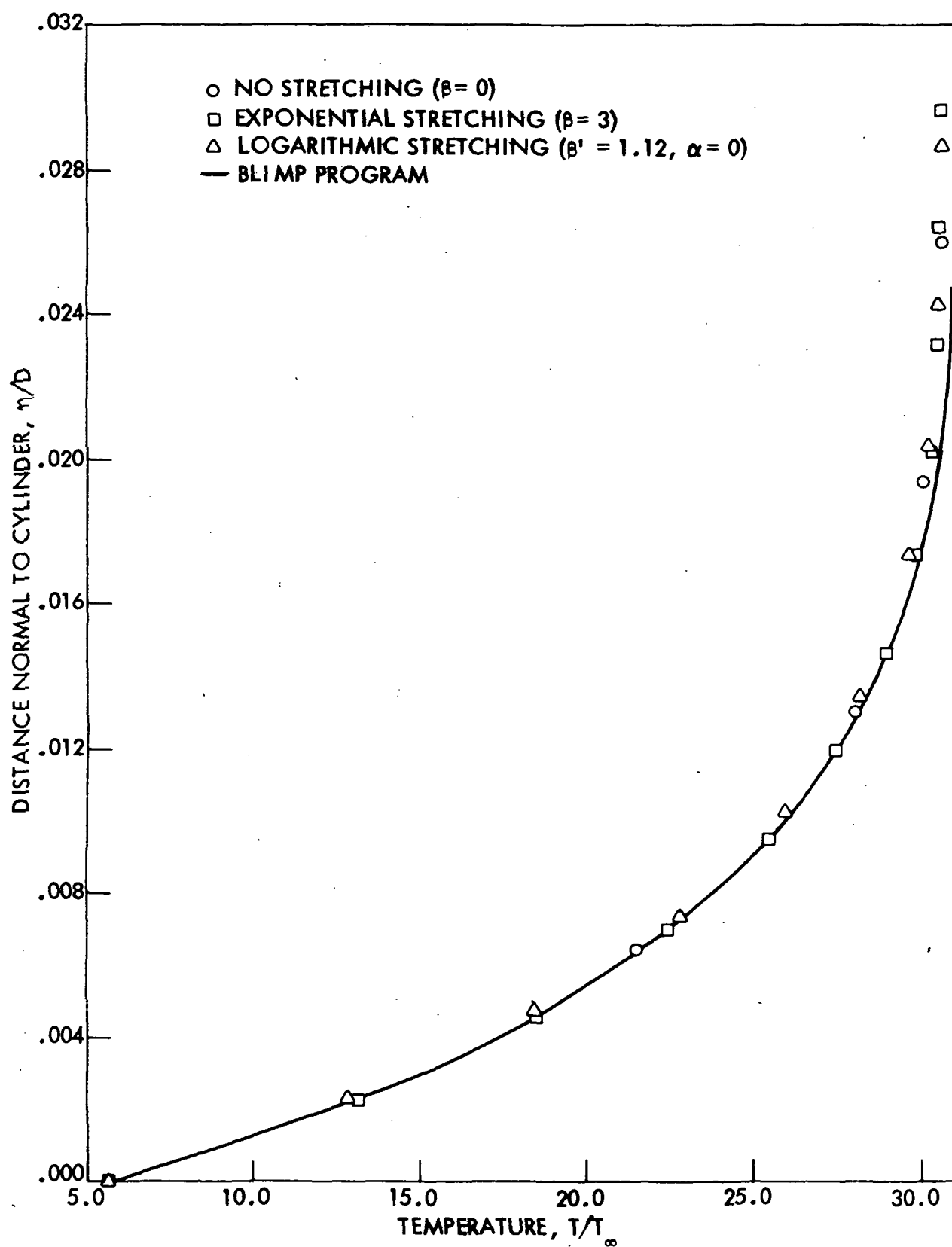exponential stretching (β = 3), an instability developed which caused
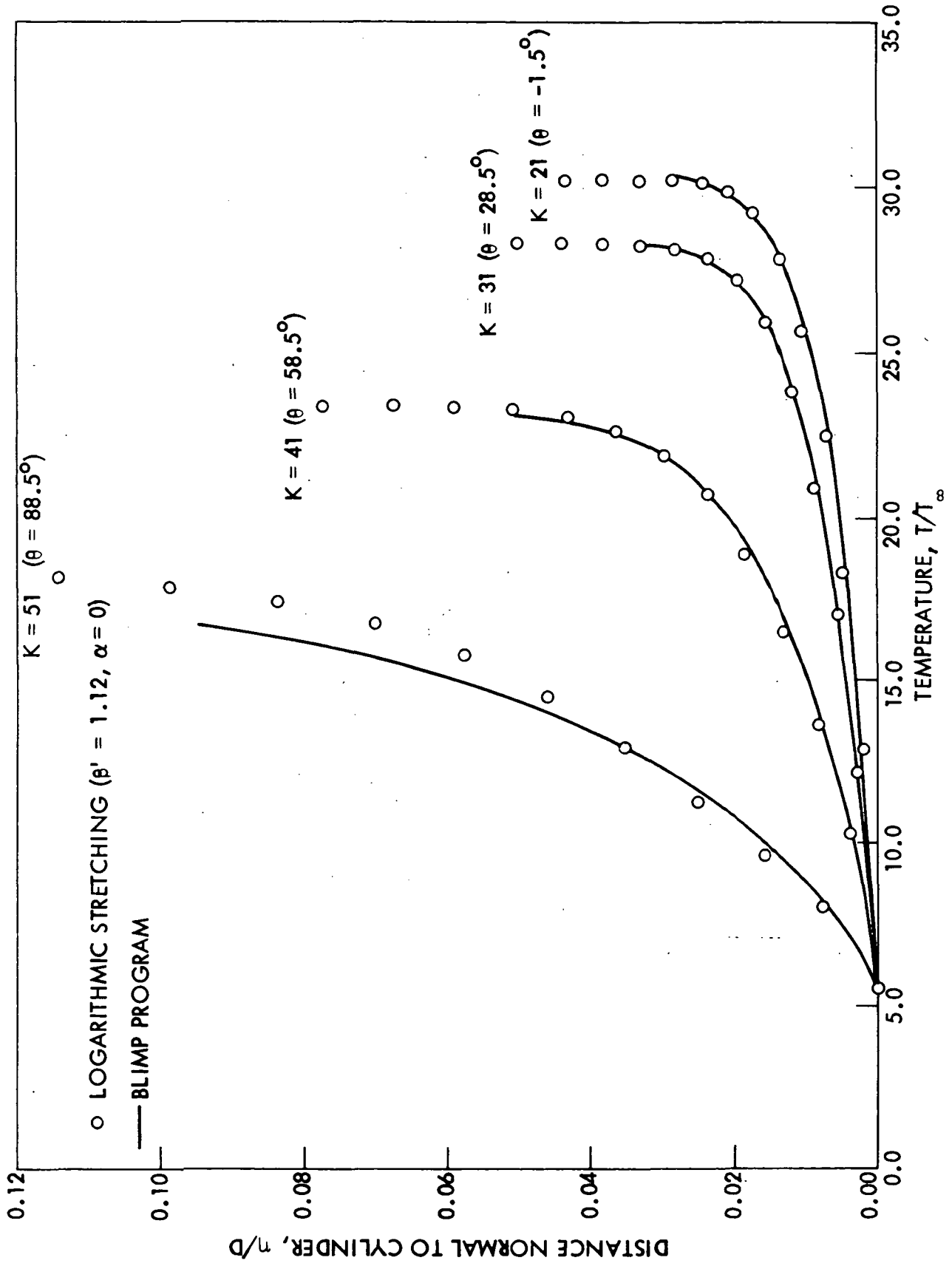
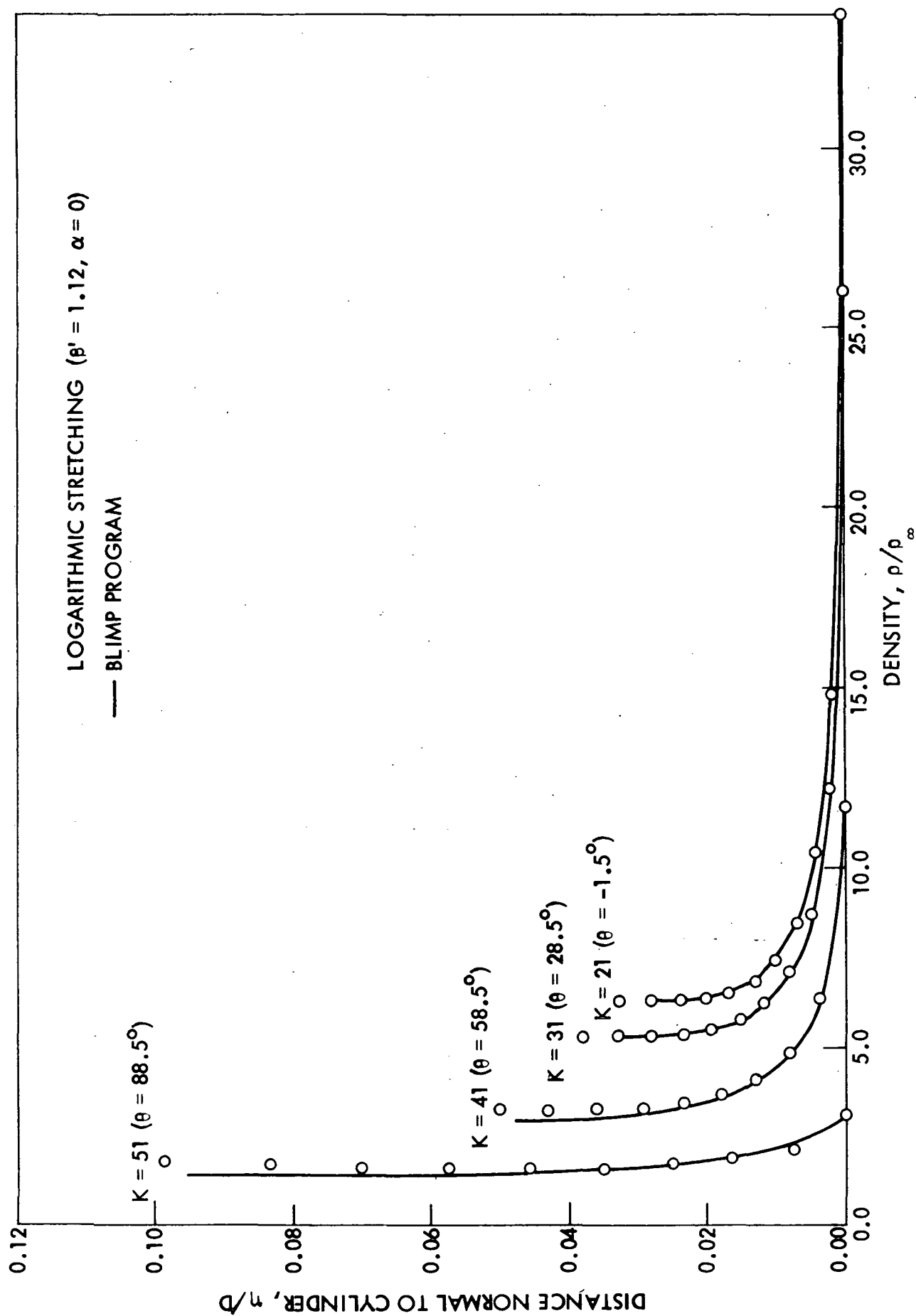Fig. 21. Temperature profiles at stagnation point.

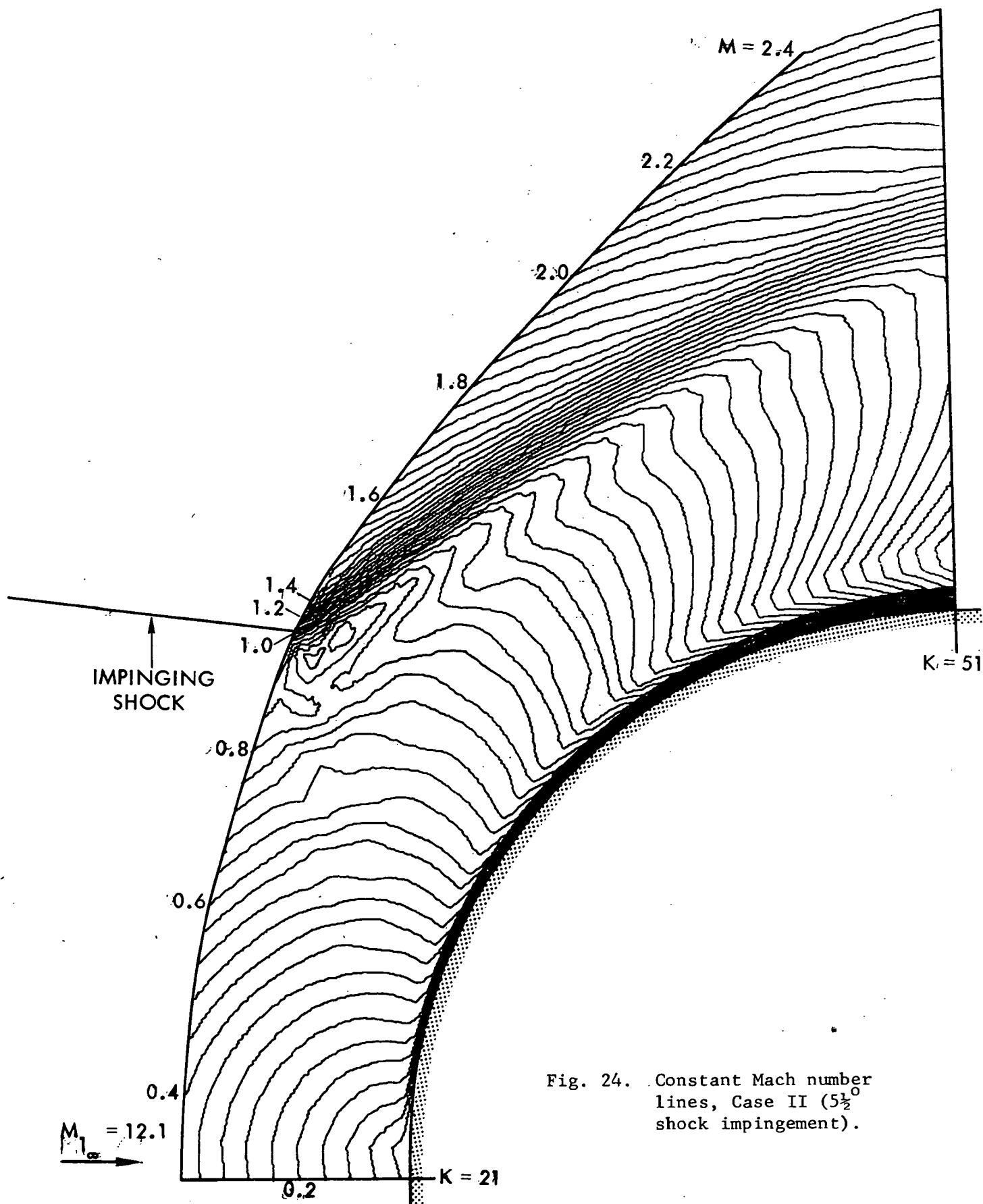Fig. 22. Temperature profiles.

Fig. 23. Density profiles.

Fig. 24. Constant Mach number
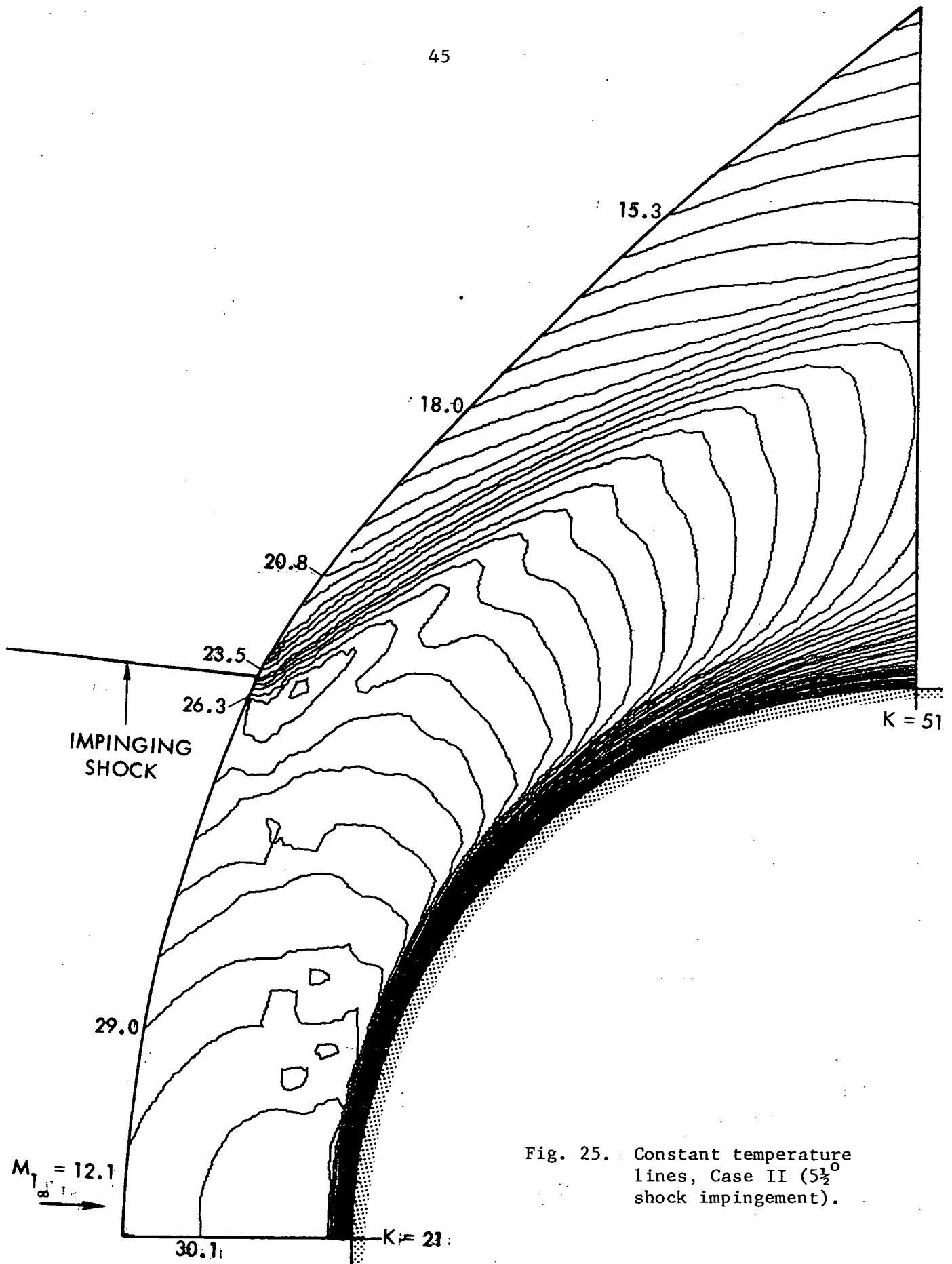lines, Case II ($5\frac{1}{2}^{\circ}$
shock impingement).

15.3

18.0

20.8

23.5

26.3

IMPINGING
SHOCK

K = 51

29.0

$M_{1_\infty} = 12.1$

30.1

K = 21

Fig. 25. Constant temperature
lines, Case II ($5\frac{1}{2}^{O}$
shock impingement).
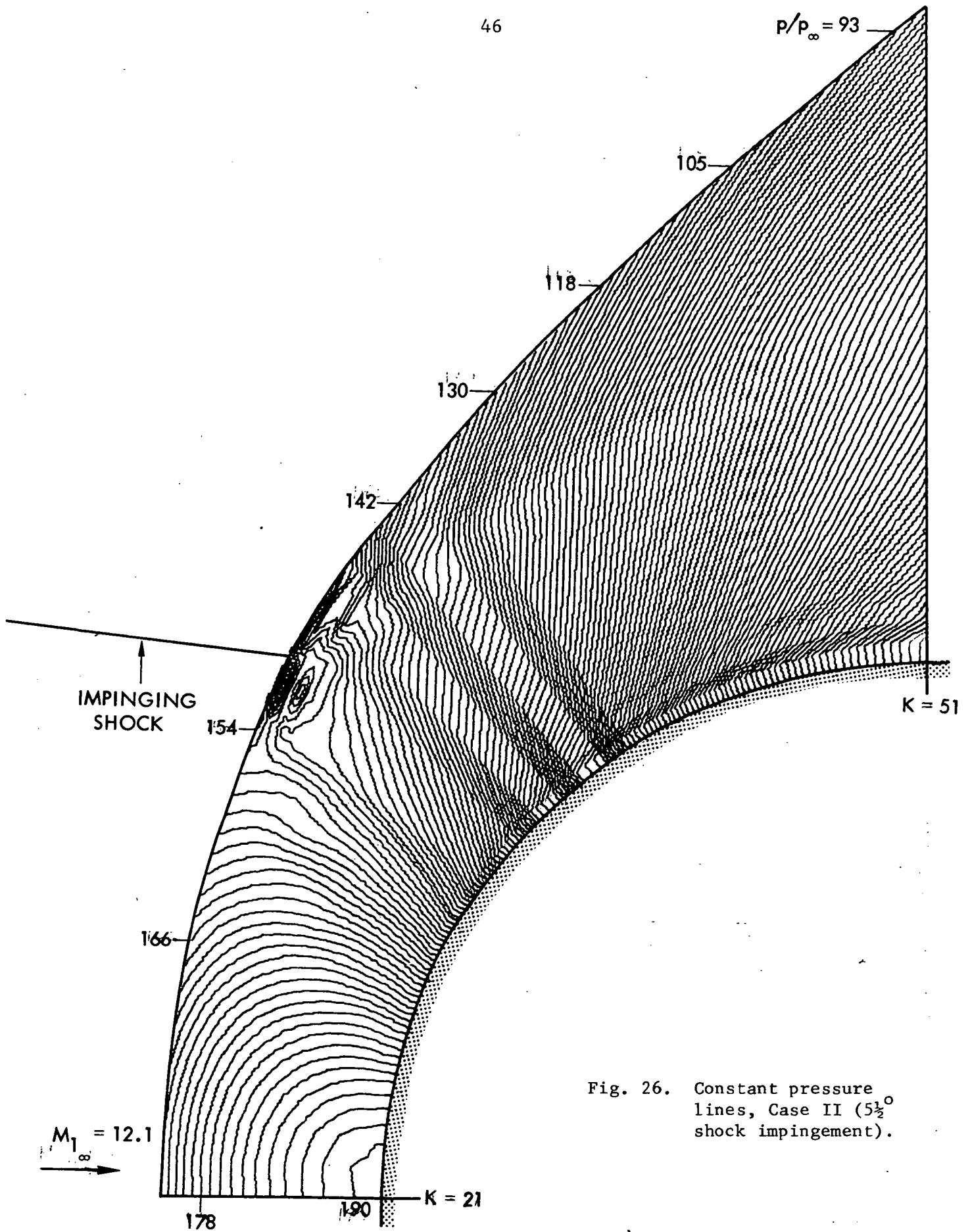
Fig. 26. Constant pressure lines, Case II (5½° shock impingement).

—·—·— NO SHOCK IMPINGEMENT

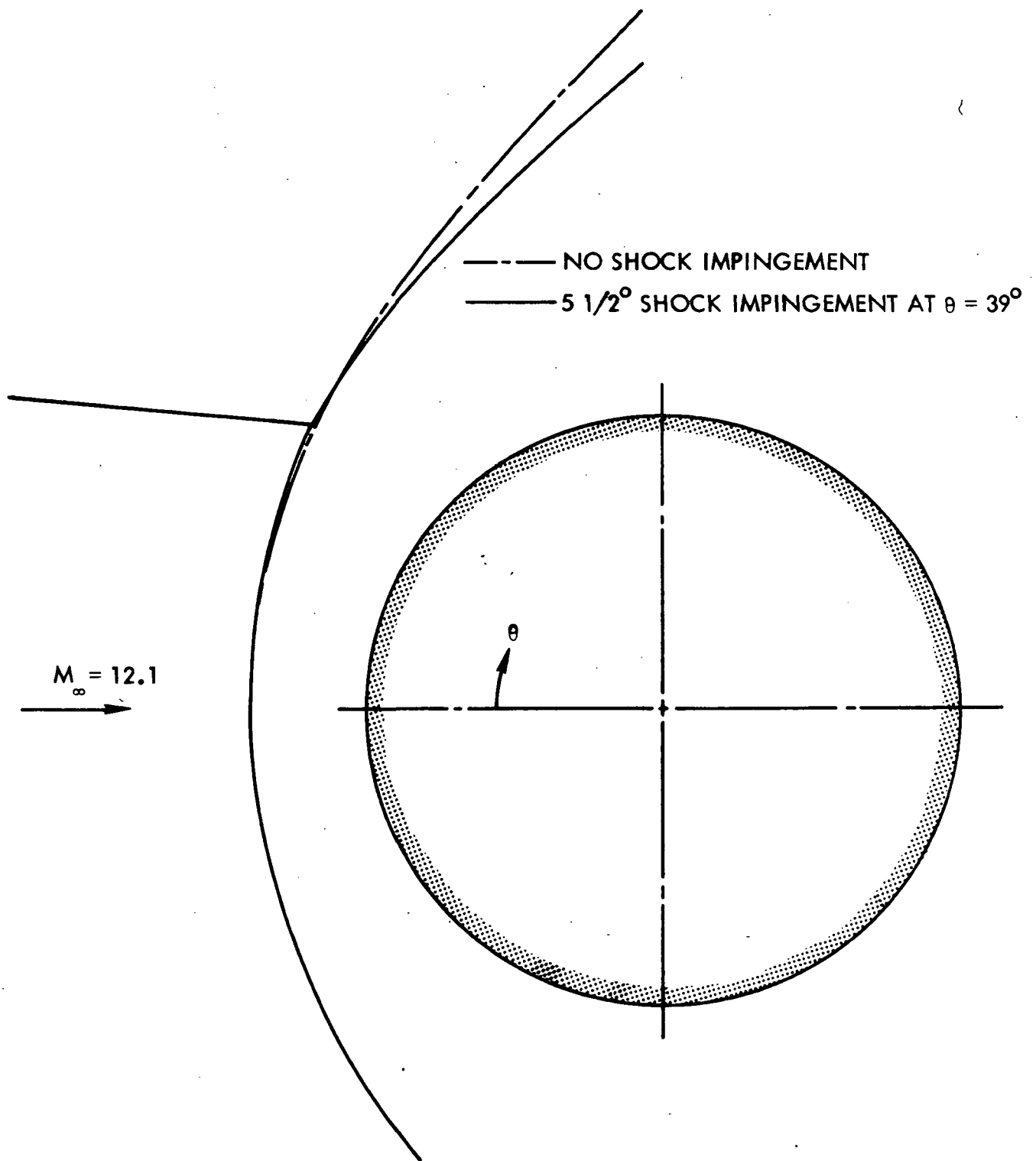——— 5 1/2° SHOCK IMPINGEMENT AT θ = 39°

θ

$M_\infty = 12.1$

Fig. 27. Shock shapes.

the solution to "blow-up". This instability was believed to be caused by the large grid spacing near the bow shock for the exponential type of stretching. This difficulty was circumvented by using logarithmic stretching with $\beta' = 1.12$ and $\alpha = 0$. This value of β' gives the same refinement at the body as the exponential type of stretching with $\beta = 3$, but the grid spacing near the bow shock is smaller for the logarithmic type of stretching.

Comparisons of the surface pressures and heat transfers between the undisturbed computation and the present shock impingement computation with logarithmic stretching are shown in Figs. 28 and 29. The incident shock causes an increase in wall pressure of 33% over the undisturbed values at the point where the outflow boundary ($k = 51$) instersects the body. The large singular value of heat transfer near $\theta = 5^{\circ}$ for the shock impingement case is the result of a numerical wave which emanates from the impingement point and hits the body. This numerical wave is evident in Fig. 25 and is believed to be caused by the finite values of shock velocity which remain near the impingement point even after the "steady-state" solution is reached. These finite values of shock velocity alternate signs between the predictor and corrector steps but have the same magnitude so that the shock position does not change after a complete time step is computed. Work is underway to eliminate this so-called "chattering" effect.

Attempts to introduce a stronger impinging shock or attempts to move the impingement point further into the subsonic region for the present flow conditions have been unsuccessful to date. Work is continuing in an effort to overcome these difficulties.
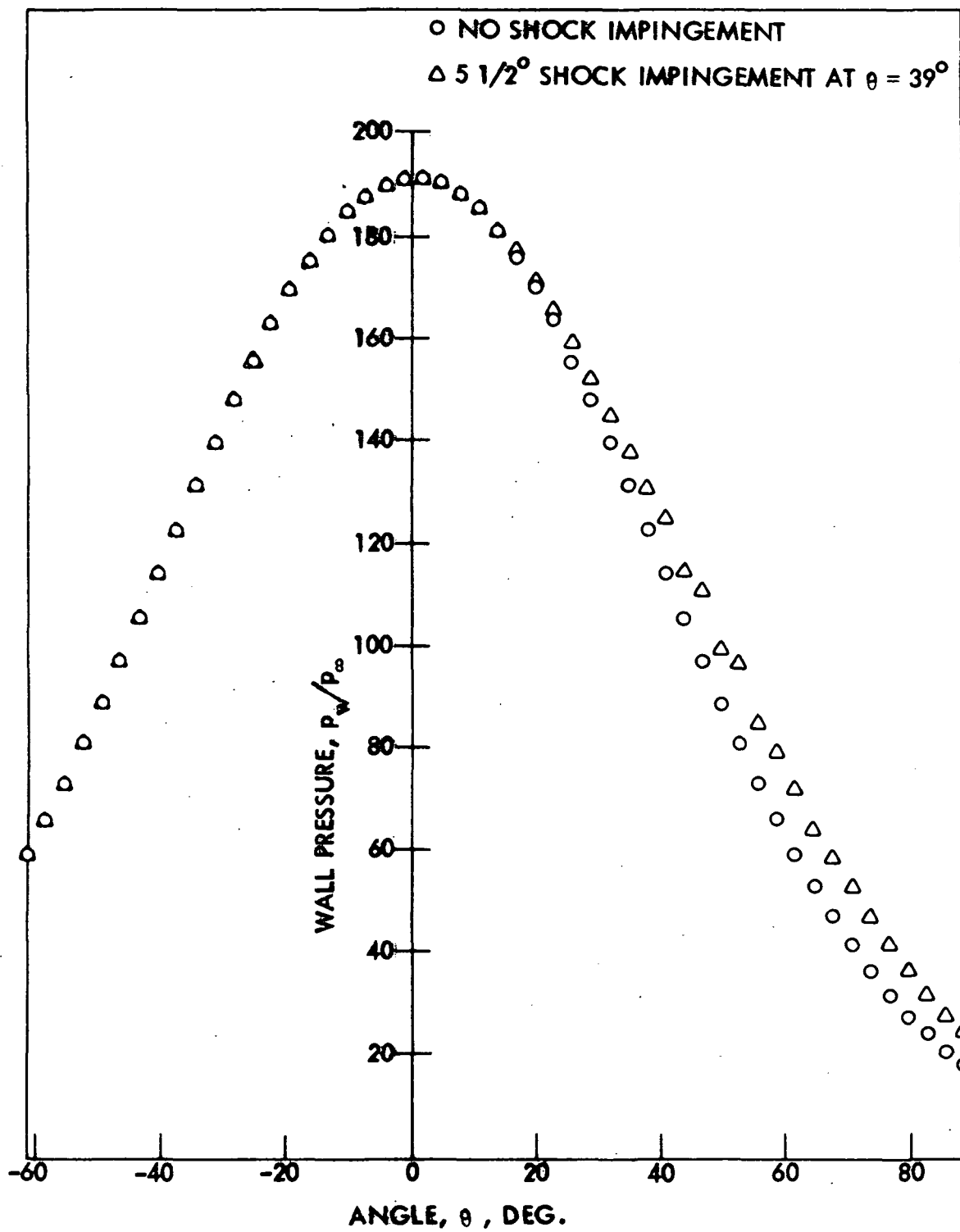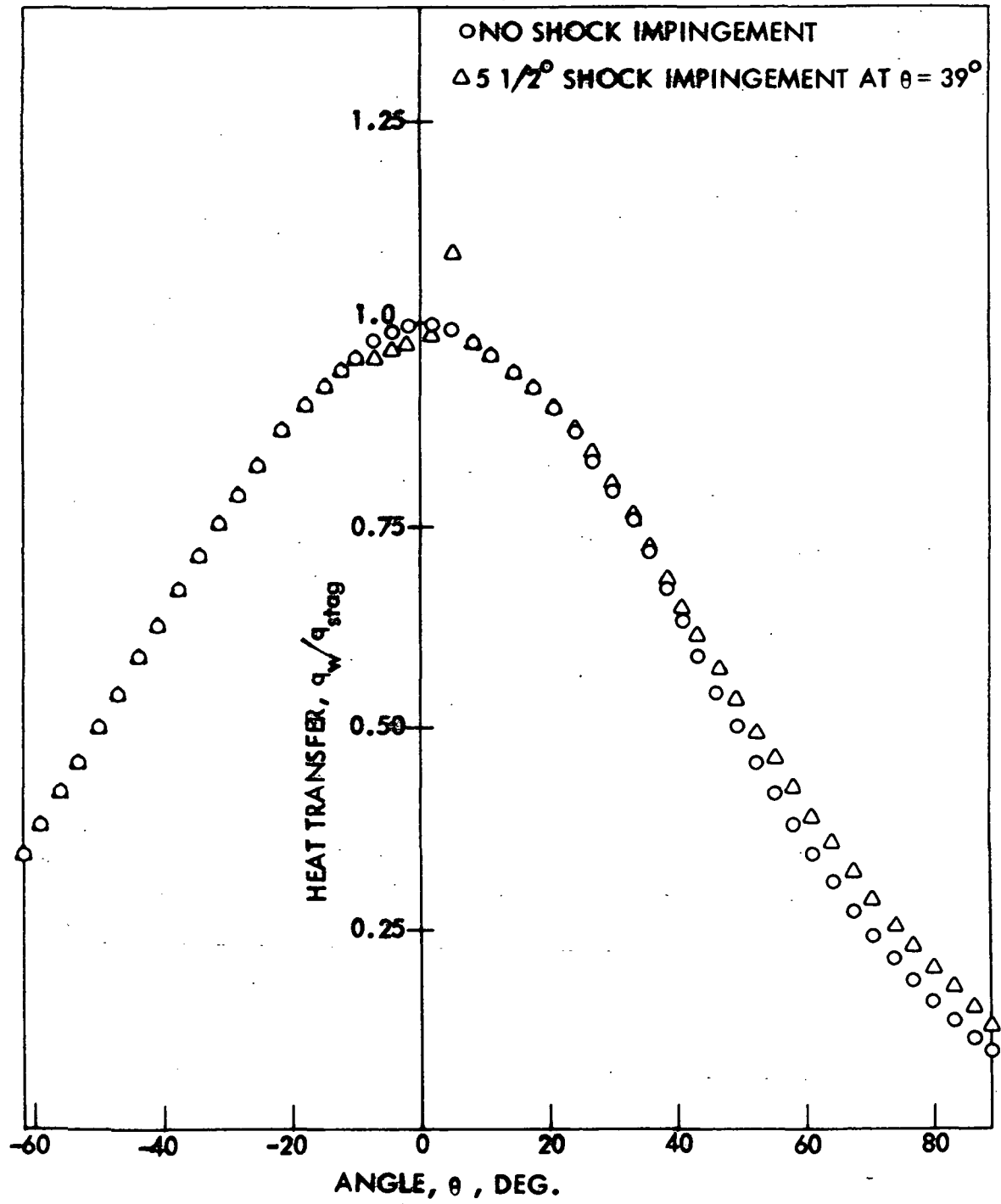
Fig. 28. Comparison of wall pressures.

Fig. 29. Comparison of heat transfers.

REFERENCES

1. Hains, F. D. and J. W. Keyes, "Shock Interference Heating in Hypersonic Flows," AIAA J., 10: 11, 1441-1447 (November 1972).

2. Edney, B. E., "Anomalous Heat Transfer and Pressure Distributions on Blunt Bodies at Hypersonic Speeds in the Presence of an Impinging Shock," FFA Rept. 115, The Aeronautical Research Inst. of Sweden, Stockholm, Sweden (February 1968).

3. Tsien, H. S., "The Equations of Gas Dynamics," Fundamentals of Gas Dynamics (H. W. Emmons, editor, Princeton University Press (1958).

4. Tannehill, J. C. and R. A. Mohling, "Development of Equilibrium Air Computer Programs Suitable for Numerical Computation Using Time-Dependent or Shock-Capturing Methods," NASA CR-2134 (September 1972).

5. Tannehill, J. C. and P. H. Mugge, "Improved Curve Fits for the Thermodynamic Properties of Equilibrium Air Suitable for Numerical Computation using Time-Dependent or Shock-Capturing Methods," ERI Report 74050, Iowa State University, Ames (February 1974).

6. Li, C. P., "Numerical Solution of Viscous Reacting Blunt Body Flows of a Multicomponent Mixture," AIAA Paper No. 73-202 (January 1973).

7. MacCormack, R. W., "The Effect of Viscosity in Hypervelocity Impact Cratering," AIAA Paper No. 69-354 (1969).

8. MacCormack, R. W., "Numerical Solution of the Interaction of a Shock Wave with a Laminar Boundary Layer," Lecture Notes in Physics, Springer-Verlag, New York, pp. 151-163 (1971).

9. Tannehill, J. C., R. A. Mohling, and J. V. Rakich, "Numerical Computation of the Hypersonic Rarefied Flow near the Sharp Leading Edge of a Flat Plate," AIAA Paper No. 73-200 (January 1973).

10. Thomas, P. D., M. Vinokur, R. Bastianon, and R. J. Conti, "Numerical Solution for the Three Dimensional Hypersonic Flow Field of a Blunt Delta Body," AIAA Paper 71-596 (1971).

11. Kutler, P., W. A. Reinhardt, and R. F. Warming, "Numerical Computation of Multishocked, Three-Dimensional Supersonic Flow Fields with Real Gas Effects," AIAA Paper 72-702 (1972).

12. Billig, F. S., "Shock-Wave Shapes around Spherical-and Cylindrical-Nosed Bodies," J. of Spacecraft and Rockets, 4: 6, 822-823 (June 1967).

13. Li, C. P., "Numerical Solutions of the Navier-Stokes Equations for the Shock Layer," Lockheed Electronics Co. Technical Report TR-675-44-459 (August 1971).

14. Broadwell, J. E. and H. Rungaldier, "Structure of the Shock Layer on Cylinders in Rarefied Gas Flow," Rarefied Gas Dynamics, (C. L. Brundin, editor) Supplement 4, Vol II, pp. 1145-1160 (1967).

15. Tong, H., "Nonequilibrium Chemistry Boundary Layer Integral Matrix Procedure, User's Manual Parts I and II," Aerotherm Corp. Report UM-73-37 (April 1973).

16. Roberts, G. O., "Computational Meshes for Boundary Layer Problems," Lecture Notes in Physics, Springer-Verlag, New York, pp. 171-177 (1971).

APPENDIX A

The transformation given below is similar to one developed by Roberts[16] and has been found in the present study to give better computational results than the previous transformation of Li[6] when an impinging shock is present. This is due to the fact that the grid spacing near the bow shock using this transformation is smaller than the grid spacing of Li's transformation for an equal grid spacing at the body. The new transformation can be used to refine the mesh near the body ($\alpha = 0$), as was done in this study, or it can be used to refine the mesh at both the body and bow shock ($\alpha = \frac{1}{2}$). The equations for this transformation are

$$\bar{y} = y$$

$$\bar{z} = \alpha + (1 - \alpha) \frac{\ln\left(\frac{\beta' + z\,(2\alpha + 1) - 2\alpha}{\beta' - z\,(2\alpha + 1) + 2\alpha}\right)}{\ln\left(\frac{\beta' + 1}{\beta' - 1}\right)} \tag{A1}$$

$$\bar{t} = t$$

The relations between the partial derivatives are given by

$$\frac{\partial}{\partial \bar{y}} = \frac{\partial}{\partial y} \tag{A2}$$

$$\frac{\partial}{\partial \bar{z}} = \frac{\left[\beta' + z(2\alpha + 1) - 2\alpha\right]\left[\beta' - z(2\alpha + 1) + 2\alpha\right]\ln\left(\frac{\beta' + 1}{\beta' - 1}\right)}{2\beta'(1 - \alpha)(2\alpha + 1)} \frac{\partial}{\partial z}$$

$$\frac{\partial}{\partial \bar{t}} = \frac{\partial}{\partial t}$$

where

$$z = \frac{(\beta' + 2\alpha)\left(\frac{\beta' + 1}{\beta' - 1}\right)^{\frac{\bar{z} - \alpha}{1 - \alpha}} - \beta' + 2\alpha}{(2\alpha + 1)\left[1 + \left(\frac{\beta' + 1}{\beta' - 1}\right)^{\frac{\bar{z} - \alpha}{1 - \alpha}}\right]} \qquad (A3)$$

and β' is related to the thickness (c) of the "boundary layer" where clustering is desired by

$$\beta' = (1 - c)^{-\frac{1}{2}} \qquad\qquad 0 < c < 1 \qquad (A4)$$